

UVIT Survey of AGN host Galaxies - I: Star Formation Scenarios

PAYEL NANDI ^{1,2} C. S. STALIN ² POULOMI DAM ^{2,3} AND D. J. SAIKIA ⁴

¹*Joint Astronomy Programme, Department of Physics, Indian Institute of Science, Bangalore 560012, India*

²*Indian Institute of Astrophysics, Block II, Koramangala, Bangalore 560034, India*

³*Dipartimento di Fisica e Astronomia, Università di Padova, Vicolo dell'Osservatorio 3, I-35122 Padova, Italy*

⁴*Inter-University Centre for Astronomy and Astrophysics, Pune 411007, India*

ABSTRACT

Circum-nuclear star formation (SF) is generally seen in galaxies hosting active galactic nuclei (AGN); however, the connection between the AGN activity and SF in them is less well understood. To explore this connection on scales of a few tens of parsec to a few tens of kiloparsec and larger, we carried out an investigation of SF in seven Seyfert type AGN and one LINER galaxy, using observations with the Ultra-Violet Imaging Telescope (UVIT) on board *AstroSat* in the near ultra-Violet (NUV; 2000–3000 Å) and far ultra-Violet (FUV; 2000–3000 Å) bands. A total of 1742 star-forming regions were identified, having size scales of 0.010 to 63.642 kpc². Considering all the galaxies, we found a positive correlation between their total surface density of SF (Σ_{SFR}) and extinction. For five galaxies, namely NGC 1365, NGC 4051, NGC 4321, NGC 5033 and NGC 6814, we found a gradual decrease of both extinction and Σ_{SFR} from the centre to the outer regions. Four sources are found to lie in the main sequence (MS) of star-forming galaxies, and the other four are away from MS. We found the ratio of the star formation rate (SFR) in the nuclear region to the total SFR to be positively correlated with the Eddington ratio. This points to the influence of AGN on enhancing the SF characteristics of the hosts. However, the impact is dominant only in the central nuclear region with no significant effect on the larger scales probed in this work.

Keywords: Active galactic nuclei (16); Seyfert galaxies (1447); Star formation (1569); Galaxy photometry (611); Ultraviolet astronomy(1736)

1. INTRODUCTION

The observational evidences of close correlation between the mass of the super-massive black holes that power active galactic nuclei (AGN) via accretion and their host galaxy properties (Ferrarese & Merritt 2000; Gebhardt et al. 2000; McLure & Dunlop 2002; Marconi & Hunt 2003; Häring & Rix 2004) clearly indicate that AGN and star formation (SF) are closely linked. This connection is believed to be via AGN feedback processes, which play an important role in the SF characteristics of their hosts from the central nuclear scales to larger galactic scales (Harrison 2017; Storch-Bergmann & Schnorr-Müller 2019; Riffel et al. 2022; Couto & Storch-Bergmann 2023; Nandi et al. 2023a; Yang et al.

2024). Theoretical studies do invoke feedback to understand galaxy evolution (Ward et al. 2022 and references therein). Also, simulations do find quenching of SF in galaxies with AGN feedback (Byrne et al. 2023). A viable feedback mechanism is AGN outflows, which can impact the SF characteristic of AGN hosts by either suppressing (negative feedback process; Harrison 2017; Hervella Seoane et al. 2023; Nandi et al. 2023b) or enhancing (positive feedback process; Maiolino et al. 2017; Gallagher et al. 2019; Zhuang et al. 2021) SF. Also, both processes could co-exist in a galaxy as has been recently observed (Zinn et al. 2013; Shin et al. 2019; García-Bernete et al. 2021).

One possibility to study the impact of AGN on the SF characteristics of their hosts is to map the star forming regions in galaxies hosting AGN and look for correlations if any between the deduced SF and AGN properties. It is natural to expect that the influence of the central AGN on their hosts could decrease from the cen-

ter to the outskirts of the galaxy (Tsai & Hwang 2015). While simulations (Bollati et al. 2023) and observations (Lammers et al. 2023) favour feedback processes to operate in the central kilo parsec scale region, its effect on kilo parsec galaxy scale is uncertain (Fiore et al. 2017). In the nearby Universe, Seyfert type AGN are ideal targets to investigate this connection as the resolution offered by ground-based imaging observations will enable one to probe SF on scales of a few hundreds of parsec to a few tens of kilo parsec. Circumnuclear SF is generally observed in this category of AGN (Davies et al. 1998; Álvarez-Álvarez et al. 2015; Hennig et al. 2018; Diniz et al. 2019). They have also been studied for SF for more than three decades in different spatial scales as well as at different wavelengths (Gu et al. 2001; Cid Fernandes et al. 2004; Davies et al. 2007; Bing et al. 2019; Riffel et al. 2022; Zhang & Ho 2023). Despite years of research, the nature of SF in AGN host galaxies *vis-a-vis* normal galaxies is not settled and highly debated. For example, in a nearby dwarf Seyfert type AGN, NGC 4395, Nandi et al. (2023a) found regions of high SF close to the center which could be due its AGN activity. Considering the far-infrared emission to be due to star formation, Rodríguez Espinosa et al. (1987) found that the far-infrared luminosities of Seyfert galaxies and star-burst galaxies are indistinguishable arguing for the bulk of the far-infrared emission in Seyfert galaxies to be due to SF. Alternatively, García-González et al. (2016) found that in a few of the Seyfert galaxies studied by them, the bulk of the nuclear far-infrared luminosity is contributed by the dust heated by the AGN. Cid Fernandes et al. (2004) studied SF history extensively in Seyfert 2 galaxies and found that they are heterogeneous and hosts a mixture of young, intermediate and old stellar populations.

To gain a comprehensive understanding of SF in galaxies, it is crucial to employ a range of wavelength bands. This is because galaxies contain diverse stellar populations and multi-phase interstellar medium (ISM), making it necessary to utilize various tracers for SF across the electromagnetic spectrum, from X-ray to radio wavelengths. In this context, radio and millimeter-wave bands serve as tracers for SF activity via their continuum and molecular line emission. On the other hand, $H\alpha$ and ultraviolet (UV) emissions act as indicators of ionizing radiation emitted by hot stars. Sometimes, the continuum UV photons interact with the surrounding gas and dust in the ISM, giving rise to infrared (IR) emissions. $H\alpha$ emission is particularly informative as it reveals the presence of stellar populations with ages ranging from 1 to 10 million years. UV emission, on the other hand, primarily traces young, massive star

clusters, providing insights into stellar populations aged between 10 and 100 million years (Kennicutt & Evans 2012). It is worth emphasizing that the presence of dust within a galaxy can diminish the intensity of UV light emitted by stars by either scattering or absorbing UV photons. Nevertheless, accounting for this extinction effect and applying suitable corrections can yield accurate and valuable results.

Until now, most studies of SF in Seyfert galaxies have been conducted in the optical, IR, or radio wavelengths using ground-based and space-based observatories. While there have been a few studies in the UV band using the Galaxy Evolution Explorer (GALEX; Martin et al. 2005), the resolution provided by GALEX is often insufficient to resolve SF on parsec scales. A limited number of studies have used the Hubble Space Telescope, which offers the capability to resolve parsec-scale structures, but it has a restricted field of view (FoV), making it observationally expensive to study a large number of sources comprehensively. To address this gap, we have undertaken a systematic investigation of the SF properties of Seyfert galaxies using the Ultraviolet Imaging Telescope (UVIT). This telescope provides moderate angular resolution, better than $1.5''$ (Tandon et al. 2020) and offers good FoV coverage, approximately $\sim 28'$ diameter. In Section 2, we describe our source selection process. Section 3 outlines our observations and data reduction procedures. In Section 4, we describe the methods we used for our analysis. In Section 5, we present our research findings on each of the objects studied in this work, the global picture of the results of this work is given in Section 6, followed by the summary in the final section. In this work, we considered a flat Λ CDM cosmology with $H_0=70 \text{ km}^{-1} \text{ s}^{-1} \text{ Mpc}^{-1}$, $\Omega_\Lambda = 0.7$ and $\Omega_m=0.3$.

2. OUR SAMPLE

Our sample of sources for this study was selected primarily from the catalogue of Véron-Cetty & Véron (2006). Our initial criteria involved the identification of objects classified as Seyferts in the Véron-Cetty & Véron (2006) catalogue with redshift $z < 0.02$. This redshift cut was imposed so that at the resolution of the Ultra-Violet Imaging Telescope (UVIT; Tandon et al. 2020), the minimum spatial scale that could be probed is about few tens of parsec. We manually inspected our sample of Seyfert type AGN in the GALEX database to assess their UV emission. Additionally, we imposed a size constraint, requiring that the selected objects have an angular size exceeding $2'$ but lesser than $12'$. We also considered some nearby low ionization nuclear emission line region (LINER) type of AGN for which UVIT ob-

servations are already available and satisfies the above criteria. This resulted in the identification of 30 objects. We have acquired observations for few sources in our sample. We aim to complete observations of the remaining targets with UVIT in the upcoming observing cycles. Results on one source in our sample, namely NGC 4395 is reported in Nandi et al. (2023a), while in this paper we report the results on another eight sources. The details of the sources are given in Table 1.

3. OBSERVATIONS AND DATA REDUCTION

The observations of our sample of sources were made using UVIT (Tandon et al. 2020), one of the payloads on board *AstroSat* (Agrawal 2006), India’s multi-wavelength astronomical observatory launched by the Indian Space Research Organization on 28 September 2015. UVIT observes simultaneously in the far ultraviolet (FUV; 1300–1800 Å) and the near ultraviolet (NUV; 2000–3000Å) over a $\sim 28'$ diameter field with a spatial resolution better than $1.5''$ in multiple filters. The FUV and NUV channels operate in the photon counting mode, while the VIS channel (VIS; 3200–5500 Å) operates in the integration mode. Images from the VIS channel are used for monitoring the drift of the satellite. For the sources in this study, we used the data available in the archives of the Indian Space Science Data Center (ISSDC¹). From ISSDC, we directly took the science ready images for further analysis in this work. These science ready images were generated by the UVIT Payload Operations Center (UVIT-POC) using the UVIT-L2 pipeline (Ghosh et al. 2022) and transferred to ISSDC for archival and dissemination. The observational details of the sources used in this study are given in Table 3. Of the eight sources, six sources have observations in both the FUV and NUV wavelengths, while two sources have observations only at FUV wavelengths. The details of the filters used are given in Table 3.

For some sources, the filter-wise combined images taken from ISSDC have exposure time smaller than the sum of the individual orbit-wise images. Also, the final astrometry has large errors. Therefore, we used the orbit-wise L2 data, aligned them and combined them filter wise using the IRAF² software package. To ensure precise astrometry of the combined images, we used the *Gaia-EDR3* catalogue (Gaia Collaboration et al. 2022), and carried out astrometry as elaborated in Nandi et al. (2023a). The measured counts/sec of the sources of interest were converted to physical units using the calibrations given in Tandon et al. (2020). For objects observed

multiple times, to generate the final combined images, we used only those orbit wise images having sufficient signal. The RGB images of the 8 sources obtained using the final FUV and NUV images from UVIT along with archival optical images are shown in Fig.1.

4. ANALYSIS

The motivation of this work is to understand the SF characteristics of the host galaxies of AGN. This involves detection of star forming regions in the galaxies. For this we used the **SExtractor** module (Bertin & Arnouts 1996) in Python. To identify star forming regions within each galaxy we adopted a 5σ threshold criterion and followed the details outlined in Nandi et al. (2023a). These identified star forming regions might have contamination from foreground objects. To remove such foreground objects, we cross-matched the identified regions with the *Gaia-DR3* (Gaia Collaboration et al. 2022) catalogue setting a cutoff in the proper motion of the regions at 10 mas/yr. If a detected SF region had a counterpart within 2 arcsecs in the *Gaia* catalogue with a proper motion exceeding 10 mas/yr, we excluded that SF region from our analysis. Thus, in total we identified 418 regions in NGC 1365, 131 regions in NGC 4051, 161 regions in NGC 4151, 340 regions in NGC 4321, 20 regions in NGC 4388, 557 regions in NGC 5033, 89 regions in NGC 6814 and 26 regions in NGC 7469. These identified regions for all the galaxies are marked and are shown in Fig. 2.

The sizes of the identified star-forming regions varied, ranging from the point spread function (PSF) of the instrument to approximately 4–5 times its size. To correct for the instrumental resolution, we adopted an assumption of elliptical light distribution within the aperture, following the approach given in Nandi et al. (2023a). These corrected apertures were subsequently utilized for further analysis. The distribution of the area of the identified star forming regions in each of the galaxies is shown in Fig. 3. We determined the flux of each of the star forming regions via aperture photometry, using **photutils** package (Bradley et al. 2020). We corrected these flux measurements for extinction. For Milky Way extinction correction, we relied on the prescription from Cardelli et al. (1989) and to correct for internal extinction, we used the UV slope (β) method (Calzetti et al. 2000). For measurements in two UV filters, one in FUV and the other in NUV, β was calculated as

$$\beta = \frac{m_{FUV} - m_{NUV}}{-2.5 \log(\lambda_{FUV}/\lambda_{NUV})} - 2.0 \quad (1)$$

Here, m_{FUV} and m_{NUV} are the magnitudes in FUV and NUV filters with wavelengths λ_{FUV} and λ_{NUV} respectively. The values of β give an idea of the dust

¹ https://astrobrowse.issdc.gov.in/astro_archive/archive/Search.jsp

² Image Reduction and Analysis Facility

Table 1. Details of the sources analysed in this work. Here, RA, DEC, redshift (z), morphology, AGN type and the extinction in V-band $A(V)$ are from NED. Here, ^a is from Parkash et al. (2018), ^b is from Bentz & Manne-Nicholas (2018), ^c is from Georgiev et al. (2016), ^d is from Andreani et al. (2018), ^e is from Sweet et al. (2018), M_* is the stellar mass and R_{25} is the radius of the galaxy to an optical surface brightness limit of 25 mag/arcsec² taken from NED.

Name	RA J2000	DEC J2000	z	scale (pc//)	Morphology	AGN type	M_* (M_\odot)	R_{25} (arcmin)	$A(V)$ (mag)
NGC 1365	03:33:36.37	-36:08:25.45	0.005	124.4	SB(s)b	Sy 1.8	10.71±0.10 ^a	5.61', 3.08', 32°	0.056
NGC 4051	12:03:09.61	44:31:52.80	0.002	41.5	SAB(rs)bc	NLSy1	10.13±0.25 ^b	2.62', 1.94', 135°	0.036
NGC 4151	12:10:32.58	39:24:20.63	0.003	62.3	(R')SAB(rs)ab	Sy 1.5	10.40±0.25 ^b	3.15', 2.13', 50°	0.074
NGC 4321	12:22:54.83	15:49:19.54	0.005	103.7	SAB(s)bc	LINER	10.83±0.28 ^c	3.71', 3.15', 30°	0.072
NGC 4388	12:25:46.75	12:39:43.51	0.008	165.8	SA(s)b	Sy 1.9	10.42 ^d	2.81', 0.64', 92°	0.091
NGC 5033	13:13:27.47	36:35:38.17	0.003	62.3	SA(s)c	Sy 1.9	11.01±0.2 ^e	5.36', 2.51', 170°	0.032
NGC 6814	19:42:40.64	-10:19:24.57	0.005	103.7	SAB(rs)bc	Sy 1.5	10.34±0.29 ^b	1.51', 1.41'	0.509
NGC 7469	23:03:15.62	08:52:26.39	0.016	331.0	(R')SAB-(rs)a	Sy 1.2	10.88±0.23 ^b	0.74', 0.54', 125°	0.188

Table 2. Summary of observations

Name	Observation ID (OBSID)	PI	Date	Filter		Exposure time(sec)	
				FUV	NUV	FUV	NUV
NGC 1365	A02.006T01.9000000776	Gulab	08/11/2016	F169M	N279N	24905	37833
	A02.006T01.9000000802	Gulab	17/11/2016				
	A02.006T01.9000000934	Gulab	28/12/2016				
NGC 4051	G05.248T01.9000000486	Stalin	11/02/2018	F172M	N219M	26444	35336
	G08.071T01.9000001888	KPSingh	11/02/2018				
NGC 4151	G06.117T01.9000001012	KPSingh	08/02/2017	F154W	N219M	67547	73548
	G06.117T01.9000001046	KPSingh	22/02/2017				
	G06.117T01.9000001086	KPSingh	17/03/2017				
	G08.064T01.9000001814	KPSingh	04/01/2018				
	G08.064T01.9000002070	KPSingh	02/05/2018				
NGC 4321	A08.003T05.9000003426	Hutchings	11/01/2020	F154W	-	6296	-
NGC 4388	A02.024T01.9000001044	Labani	21/02/2017	F154W	N245M	13520	13621
NGC 5033	G06.087T04.9000001028	Stalin	14/02/2017	F148W	N279N	2930	2948
NGC 6814	A05.037T01.9000003140	Pranoti	02/09/2019	F154W	-	46782	-
NGC 7469	G08.071T02.9000001620	KPSingh	18/10/2017	F172M	N245M	34493	50032

Table 3. The details of the filters used in this work (Tandon et al. 2020). Here, λ_{mean} and $\Delta\lambda$ are the mean wavelength and band width in Å.

Filter Name	λ_{mean} (Å)	$\Delta\lambda$ (Å)
F148W	1481	500
F154W	1541	380
F169M	1608	290
F172M	1717	125
N219M	2196	270
N245M	2447	280
N279N	2792	90

obscuration in the star forming regions. Using the cal-

culated β , we estimated the colour excess, $E(B-V)$ using the following relation

$$E(B-V) = (\beta + 2.616)/4.684 \quad (2)$$

The distribution of the $E(B-V)$ values for the identified star forming regions are given in Fig. 4. We estimated the internal extinction at any particular wavelength, λ as

$$A_\lambda = 0.44 \times E(B-V) \times k'(\lambda) \quad (3)$$

where, $k'(\lambda)$ is from Calzetti et al. (2000).

In cases where NUV data from UVIT were unavailable, we calculated the UV slope using two FUV filters. For regions where neither FUV and NUV filters nor two

FUV filters were available from UVIT, we utilized the GALEX FUV and NUV images. In such instances, we convolved the instrument-corrected aperture with the GALEX PSF and employed those apertures to determine the extinction correction. The spatial and radial variations of internal extinction for our sample of galaxies are shown in Fig. 5.

After getting the extinction value for each SF region, we calculated the intrinsic luminosities of the star forming regions and used them to estimate the star formation rate (SFR) in NUV and FUV wavelengths as follows (Salim et al. 2007).

$$\log(SFR_{FUV}(M_{\odot}yr^{-1})) = \log[L_{FUV}(WHz^{-1})] - 21.16 \quad (4a)$$

$$\log(SFR_{NUV}(M_{\odot}yr^{-1})) = \log[L_{NUV}(WHz^{-1})] - 21.14 \quad (4b)$$

We calculated the surface density of star formation rate (Σ_{SFR}) by taking the ratio of the SFR to the area of the star forming regions. The spatial and radial variations of Σ_{SFR} values for our sample of sources are shown in Fig. 6.

5. NOTES ON INDIVIDUAL SOURCES

5.1. NGC 1365

NGC 1365 at a redshift $z=0.005$ (de Vaucouleurs et al. 1991), is a face-on barred spiral galaxy of SB(s)b type (de Vaucouleurs et al. 1991) and harbouring a Seyfert 1.8 type AGN (Maiolino & Rieke 1995) with a black hole of mass $M_{BH} \sim 10^{6.5} M_{\odot}$ (Risaliti et al. 2009). NGC 1365 with an X-ray luminosity of $L_{2-10keV} = 10^{42}$ erg s^{-1} (Risaliti et al. 2005) is variable in X-rays, exhibiting variability on timescales of hours to years (Brennan et al. 2013). Notably, NGC 1365 is host to a rich population of star clusters and is a prominent galaxy within a 30 Mpc distance (Whitmore et al. 2023). At radio frequencies, detection of a ring-like structure in the circumnuclear region with multiple knots of emission was reported by Saikia et al. (1994). This was followed by a more detailed study which showed the knots of emission to have a non-thermal spectrum, and a suggestion of a possible jet-like structure along a $PA \sim 125^{\circ}$ (Sandqvist et al. 1995). Stevens et al. (1999) confirm the non-thermal nature of the knots and suggest that these are mostly due to multiple supernova remnants (SNRs). They also suggest that the jet-like structure could be due to a nuclear bar which extends to the ring.

We identified 418 star forming regions with the faintest region of 23.56 mag in FUV, while the brightest region has a brightness of 13.70 mag in the same FUV band. In the NUV, the faintest and the brightest

SF regions have brightness of 23.81 mag and 12.79 mag respectively. These star forming regions span a broad range of sizes. Their sizes range from $0.042 - 11.93$ kpc^2 , with average and median values of 0.713 kpc^2 and 0.215 kpc^2 respectively.

We found the color excess, $E(B-V)$ to vary from 0.019 mag to 0.783 mag, with an average of 0.212 mag and a median of 0.195 mag. In FUV band, the extinction ranged from 0.08 mag to 3.428 mag, with an average of 0.93 mag and a median of 0.86 mag. Meanwhile, in the NUV band, the extinction values range from 0.06 mag to 2.51 mag, with a median of 0.63 mag and an average of 0.68 mag. We found high extinction in the inner regions compared to the outer regions (see Fig. 5). The Σ_{SFR} for the star-forming regions in NGC 1365 varied between $1.268 \times 10^{-3} - 22.96 \times 10^{-2} M_{\odot} yr^{-2} kpc^{-2}$ in the FUV band, with an average Σ_{SFR} of $8.91 \times 10^{-3} M_{\odot} yr^{-1} kpc^{-2}$. Similarly, in the NUV band, we found the Σ_{SFR} values to vary between 9.72×10^{-4} and $55.62 \times 10^{-2} M_{\odot} yr^{-1} kpc^{-2}$, with a average of $11.19 \times 10^{-3} M_{\odot} yr^{-1} kpc^{-2}$. We found the distribution of the Σ_{SFR} values in both FUV and NUV to be similar. We found the extinction and Σ_{SFR} to decrease radially outwards, as can be seen in Fig. 5 and Fig. 6 respectively. The details of the SF regions are given in Table 6.

5.2. NGC 4051

NGC 4051, an intermediate barred spiral galaxy with a morphological type of SAB(rs)bc (de Vaucouleurs et al. 1991; Evans et al. 1996), is at a redshift of $z = 0.002$ (Véron-Cetty & Véron 2006). It is a narrow line Seyfert 1 galaxy (Khachikian & Weedman 1974) and powered by a black hole of mass $6 \times 10^5 M_{\odot}$ (Seifina et al. 2018). It is luminous in X-rays with $L_{2-10keV} = 2.7 \times 10^{41}$ erg s^{-1} (Pounds et al. 2004), and is known to be variable across wavelengths and timescales (Peterson et al. 2000; McHardy et al. 2004; Jones et al. 2011; Kumari et al. 2023). High-resolution observations at radio frequencies such as with the VLA A-array at 8.4 GHz show a core and two distinct components on opposite sides, while lower-resolution observations do not resolve well the inner triple but exhibits more diffuse extended emission (e.g. Jones et al. 2011). Unlike at X-ray wavelengths, they do not find evidence of significant variability of the core at radio frequencies. From continuum-subtracted $H\alpha$ images, Evans et al. (1996) identified numerous HII knots within its spiral arms.

We detected 131 star-forming regions having FUV brightness between 23.97 mag (the faintest) and 16.55 mag (the brightest). Similarly, in the NUV band, the star forming regions varied in brightness between 24.40 mag at the faintest end and 16.69 mag at the brightest

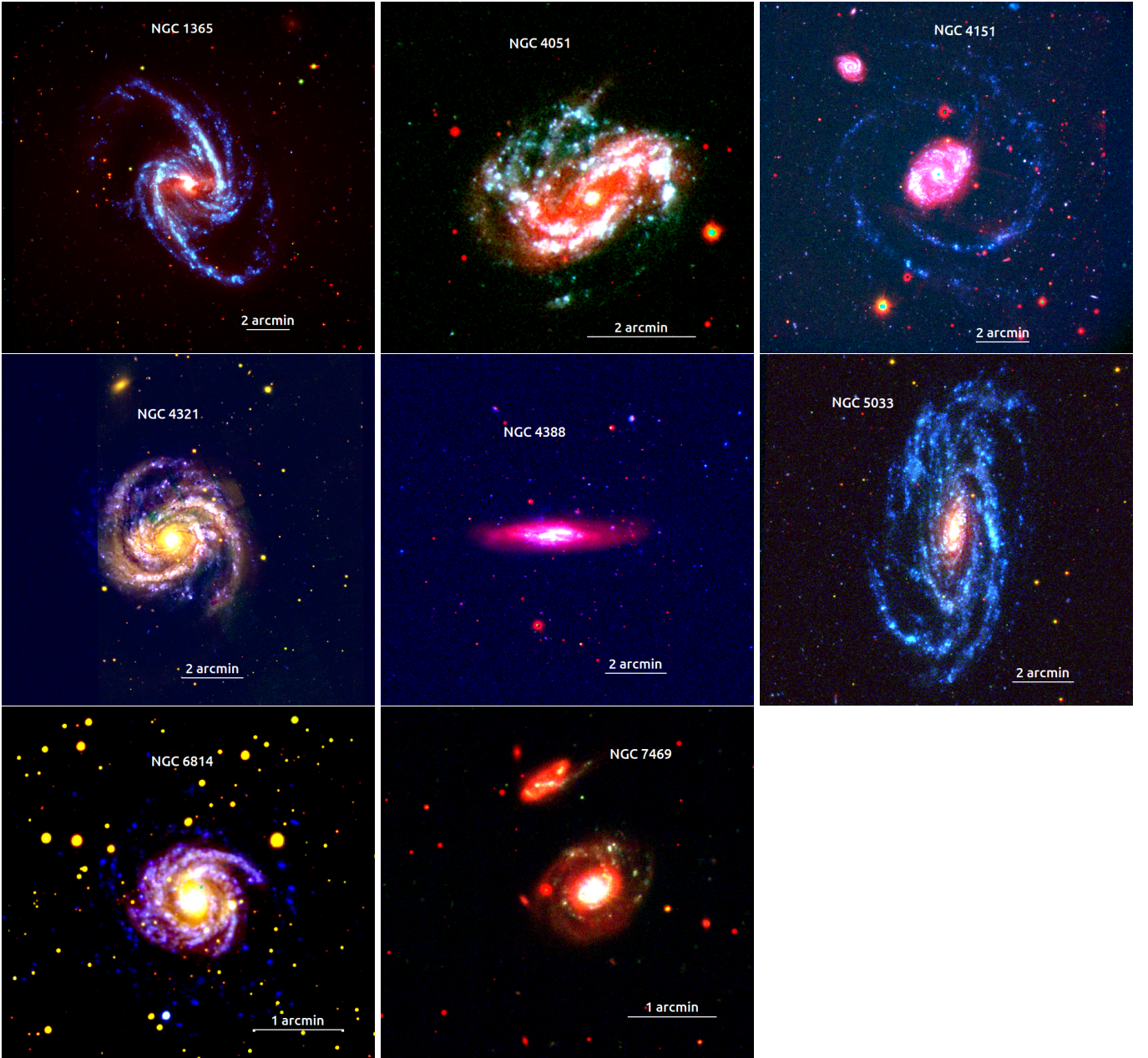


Figure 1. RGB images of the sources. Here, red is Pan-STARRS r band (except for NGC 1365 where it is from the Decadal legacy survey), green is UVIT NUV (except for NGC 4321 and NGC 6814 where it is Pan-STARRS g-band) and blue is UVIT FUV.

end. The areas of these star forming regions have a wide range, varying from 0.046 kpc^2 to 2.144 kpc^2 , with the average and median value of 0.341 kpc^2 and 0.207 kpc^2 respectively.

We found the $E(B-V)$ values to span a wide range from -0.357 mag to 0.418 mag , with an average of value of -0.046 mag and a median value of -0.038 mag . Extinction in the FUV band is found to vary between -1.51 mag and 1.77 mag , while, in the NUV band, we found the extinction values to vary between -1.32 mag and

1.55 mag , with mean and median values of -0.17 mag and -0.14 mag , respectively.

We found the Σ_{SFR} of the star forming regions to have a wide range between 1.09×10^{-4} and $42.79 \times 10^{-4} \text{ M}_{\odot} \text{ yr}^{-1} \text{ kpc}^{-2}$ in the case of FUV and between 8.1×10^{-5} and $41.22 \times 10^{-4} \text{ M}_{\odot} \text{ yr}^{-1} \text{ kpc}^{-2}$ in the case of NUV. The average Σ_{SFR} in the FUV and NUV bands are $7.72 \times 10^{-4} \text{ M}_{\odot} \text{ yr}^{-1} \text{ kpc}^{-2}$ and $6.98 \times 10^{-4} \text{ M}_{\odot} \text{ yr}^{-1} \text{ kpc}^{-2}$ respectively. We found the Σ_{SFR} values to be similar in both FUV and NUV bands.

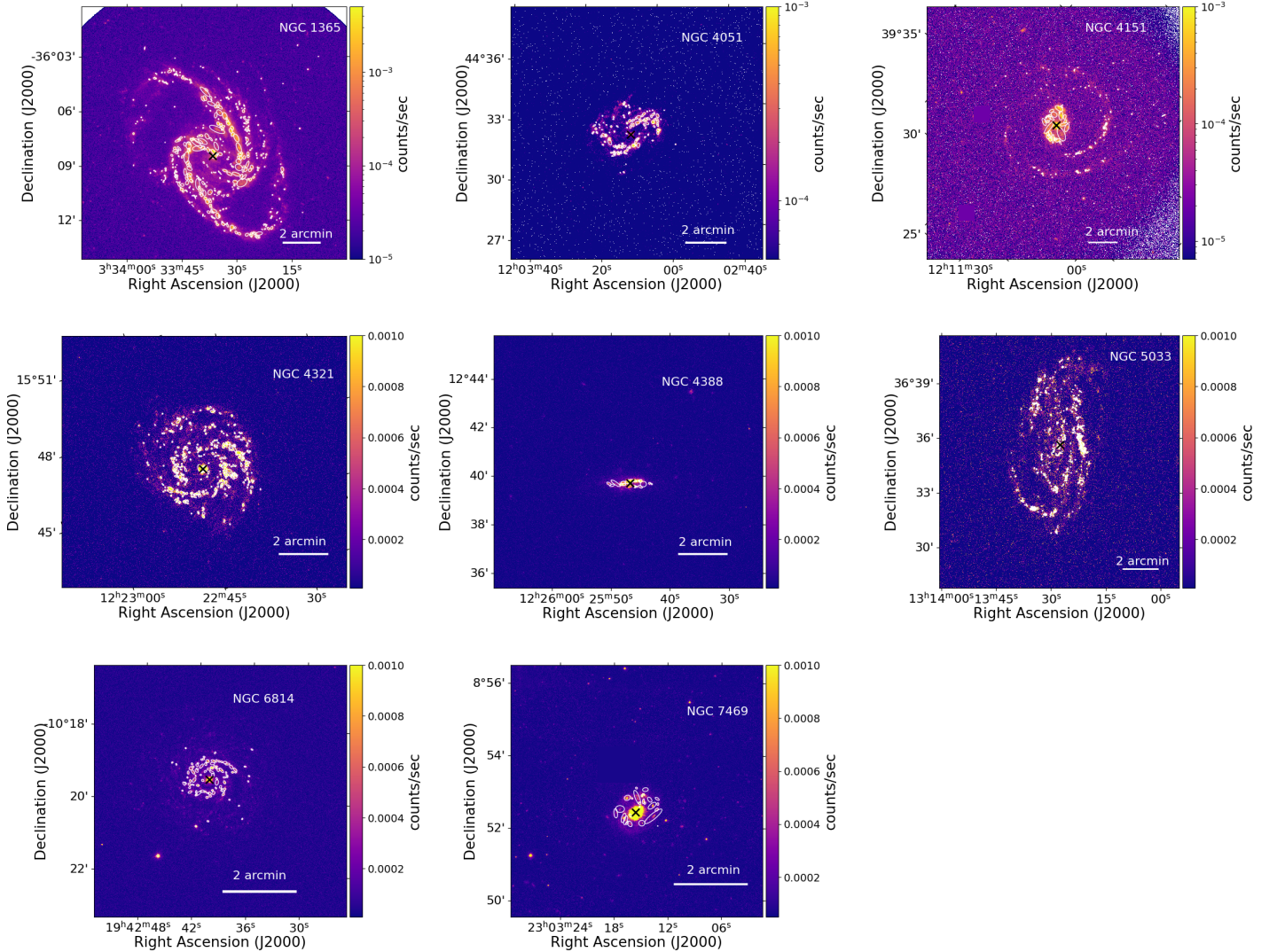


Figure 2. FUV images of the objects with the identified star-forming regions marked in white ellipses. The central AGN is marked as a black cross.

5.3. NGC 4151

NGC 4151 with a well-defined spiral pattern and a central bulge (de Vaucouleurs et al. 1991; Mundell et al. 1999) is an intermediate face-on spiral galaxy with a morphology of (R')SAB(rs)ab. It hosts a Seyfert 1.5 AGN (Véron-Cetty & Véron 2006), situated at a redshift of $z=0.0033$ (Wolfinger et al. 2013) and powered by a black hole of mass $4.57 \times 10^7 M_{\odot}$ (Bentz et al. 2006). Its X-ray luminosity ranges between $(1.3-2.1) \times 10^{42} \text{ erg s}^{-1}$ (Wang et al. 2010) and has been studied for variability over a wide range of wavelengths. It has a two-sided radio jet, and the gas-rich spiral arms, along with the bar, are prominently visible in HI images (Bosma et al. 1977). The outer spiral arms are clearly visible in both FUV and NUV images as can be seen in Fig. 1 and Fig. 2. These two distinct spiral arms are not

prominent in the optical band, which are nicely traced by HI observation (Pedlar et al. 1992). The radio structure of NGC 4151 has been studied for decades. It exhibits a two-sided jet with multiple components along a $PA \sim 77^{\circ}$, with one of the components (C4) coincident with the optical nucleus of the galaxy. C4, which is presumably associated with the supermassive black hole at its centre, was found to vary at radio frequencies, but no significant motion was detected between C4 and the nearby C3 component over a 22-year period (Williams et al. 2017).

We detected 161 star forming regions. The faintest and the brightest star-forming regions identified by us in the FUV image of NGC 4151 have a magnitude of 23.76 mag and 16.36 mag, respectively. Similarly, in the NUV band, the faintest and the brightest star-forming

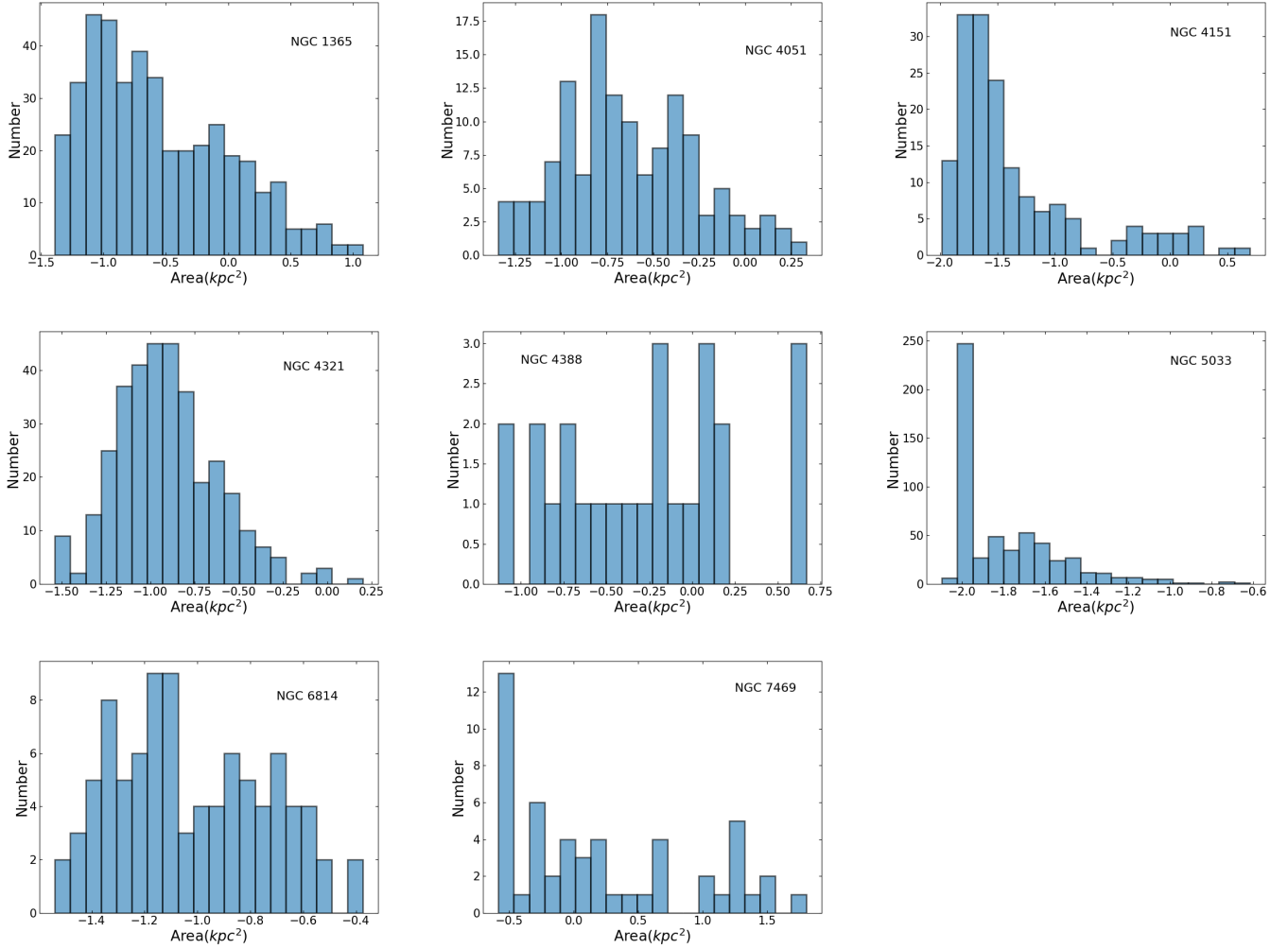


Figure 3. Distributions of the area (log scale) of the identified star-forming regions in the sources studied in this work. The names of the sources are given in their respective panels.

regions detected have a brightness value of 23.91 mag and 16.25 mag respectively. These star-forming regions have a wide range of area between 0.010 kpc^2 to 4.921 kpc^2 , with an average and median area of 0.188 kpc^2 and 0.027 kpc^2 respectively. We found the color excess, $E(B-V)$ to vary between 0.032 mag and 2.446 mag, with an average value of 0.252 mag and a median value of 0.227 mag. Extinction in the FUV band varied between 0.15 mag to 3.21 mag, with an average of 1.13 mag and a median of 1.02 mag, while in the NUV band, extinction varied from 0.12 mag to 2.66 mag, with a median of 0.94 mag and an average of 0.843 mag.

The estimated Σ_{SFR} of these SF regions exhibited a wide range, with Σ_{SFR} values in the FUV band varying from 8.55×10^{-4} to $0.05 \text{ M}_{\odot} \text{ yr}^{-1} \text{ kpc}^{-2}$. The average Σ_{SFR} in the FUV band is $48.40 \times 10^{-4} \text{ M}_{\odot} \text{ yr}^{-1} \text{ kpc}^{-2}$. In the NUV band, Σ_{SFR} values ranged between 7.72×10^{-4} and $0.07 \text{ M}_{\odot} \text{ yr}^{-1} \text{ kpc}^{-2}$ with an average Σ_{SFR} of

$57.11 \times 10^{-4} \text{ M}_{\odot} \text{ yr}^{-1} \text{ kpc}^{-2}$. The detailed properties of the 440 the star forming regions are given in Table 8.

5.4. NGC 4321

NGC 4321, classified as a late-type, nearly face-on grand design spiral galaxy with a SAB(s)bc morphology (de Vaucouleurs et al. 1991), is at a redshift of $z = 0.00524$ (Allison et al. 2014) and is powered by a black hole of mass $(2.5 \pm 0.2) \times 10^7 \text{ M}_{\odot}$ (Sarzi et al. 2002). It has two bars and a circumnuclear ring (Garcia-Burillo et al. 1998). It is categorized as HII/LINER and exhibits a relatively high X-ray luminosity, exceeding $1.9 \times 10^{40} \text{ erg s}^{-1}$ (González-Martín et al. 2009). In the radio, the image made with the Effelsberg telescope with an angular resolution of $\sim 71 \text{ arcsec}$ shows a bright central region and an extended disk (Urbanik et al. 1986). Higher-resolution observations with the VLA with an angular resolution of 2 arcsec showed the central region

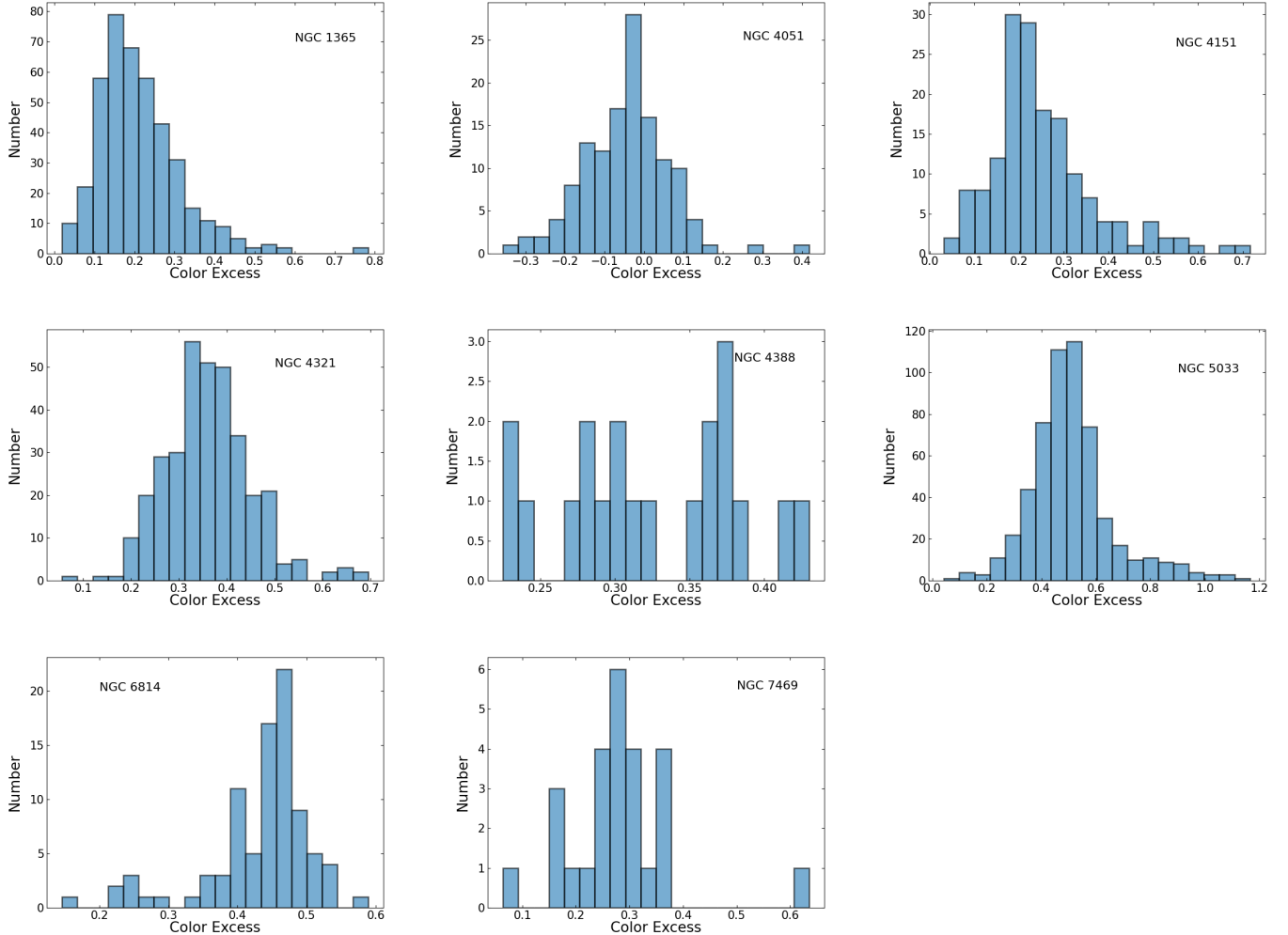


Figure 4. Distributions of $E(B-V)$ of the identified star-forming regions in the sources studied in this work. The names of the sources are given in their respective panels.

to have a roughly circular structure with an angular extent of ~ 20 arcsec. Radio emission appears to peak at the optical nucleus and also at an enhanced region ~ 7 arcsec to the east near an optical condensation, besides emission from SN1979c (Weiler et al. 1981). Moreover, strong activity has been observed across optical and radio wavelengths, leading to the classification of NGC 4321 as a transition galaxy, bridging the gap between normal and AGN galaxies (Immler et al. 1998).

NGC 4321 has giant molecular associations in various regions, including the bar, spiral arms, and circumnuclear ring (Pan & Kuno 2017). It has been observed that SF is most active within the circumnuclear ring, with lower activity occurring in the inter-arm regions (Pan & Kuno 2017). SF in the circumnuclear region or nuclear rings is attributed to bursts triggered by the Inner Lindblad resonance (Arsenault 1989). Additionally, $H\alpha$ emission is prominent on the leading side of the

bar and spiral arms, contributing to the understanding of star-forming regions in the galaxy (Pan & Kuno 2017). Further studies, such as those by Ferreras et al. (2012), have investigated young star-forming regions in the NUV and optical ranges. While these studies confirmed the association of $H\alpha$ emission with the nuclear region, they did not find a significant correlation between the distance from these regions and the age or dust content.

We identified 340 star-forming regions in NGC 4321. These regions have a wide range in brightness with values ranging between 22.19 mag and 13.92 mag in the FUV band. They have a range of sizes from 0.029 kpc^2 to 1.587 kpc^2 , with an average area of 0.159 kpc^2 and a median of 0.116 kpc^2 . The $E(B-V)$ values within these regions range between 0.056 mag and 0.695 mag, with an average and median values of 0.361 mag and 0.356 mag respectively. We found the extinction in the FUV

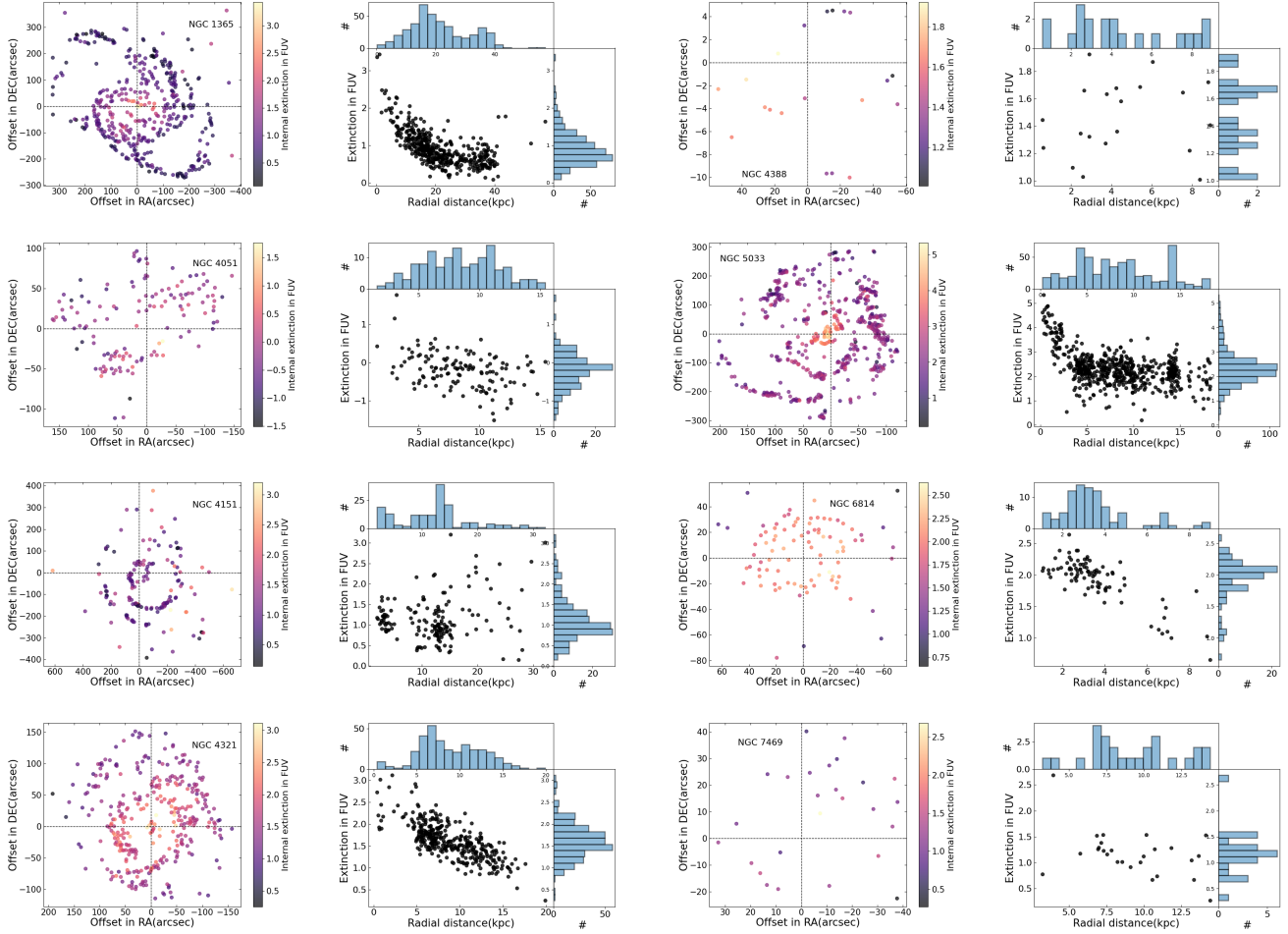


Figure 5. Spatial (left panel) and radial (right panel) variation of internal extinction for each source.

band to cover a wide range from 0.25 mag to 3.11 mag, with an average and median of 1.62 mag and 1.59 mag, respectively.

The Σ_{SFR} within these star formation regions in the FUV band have a wide range from 5.82×10^{-3} to $55.17 \times 10^{-2} M_{\odot} \text{ yr}^{-1} \text{ kpc}^{-2}$, with an average Σ_{SFR} of $3.43 \times 10^{-2} M_{\odot} \text{ yr}^{-1} \text{ kpc}^{-2}$. Both extinction and Σ_{SFR} were found to show a gradual decline from the center towards the outer regions of the galaxy as can be seen in Fig. 5 and Fig. 6.

5.5. NGC 4388

NGC 4388 is a nearly edge-on spiral galaxy, classified as type SA(s)b with a major axis position angle of 91° (Paturel et al. 2003; de Vaucouleurs et al. 1991). Located at a distance of approximately 37.55 Mpc corresponding to a redshift of $z=0.00842$ (Lu et al. 1993), this galaxy exhibits a short bar whose strength depends on the eccentricity of stellar or gas orbits (Veilleux et al. 1999). At its center, NGC 4388 hosts a type 2 Seyfert AGN with a supermassive black hole of mass

$(8.4 \pm 0.2) \times 10^6 M_{\odot}$ (Tueller et al. 2008; Kuo et al. 2011). It is a strong X-ray source, with an X-ray luminosity of $L_{2-10\text{keV}} = 1 \times 10^{42} \text{ erg s}^{-1}$ (Forster et al. 1999). VLA observations have revealed an elongated blob with an extent of ~ 13 arcsec to the north of the galaxy and a collimated structure of ~ 2.8 towards the south, the observed asymmetry possibly being due to an asymmetric distribution of ISM (Hummel & Saikia 1991). More recently Sargent et al. (2024) have made a detailed study with the VLA in both total intensity and linear polarization and have suggested that the radio continuum emission is due to AGN winds interacting with the local ISM.

NGC 4388 also exhibits significant dust obscuration, with dust bands extending to approximately 1.5 kpc from the center of the disk (Falcke et al. 1998). Studies have shown that the galaxy possesses a truncated HI disc and gas components outside the plane, suggesting a possible interaction with the intergalactic medium (Singh et al. 2019). This interaction is believed to have involved ram pressure stripping, resulting in the loss of approxi-

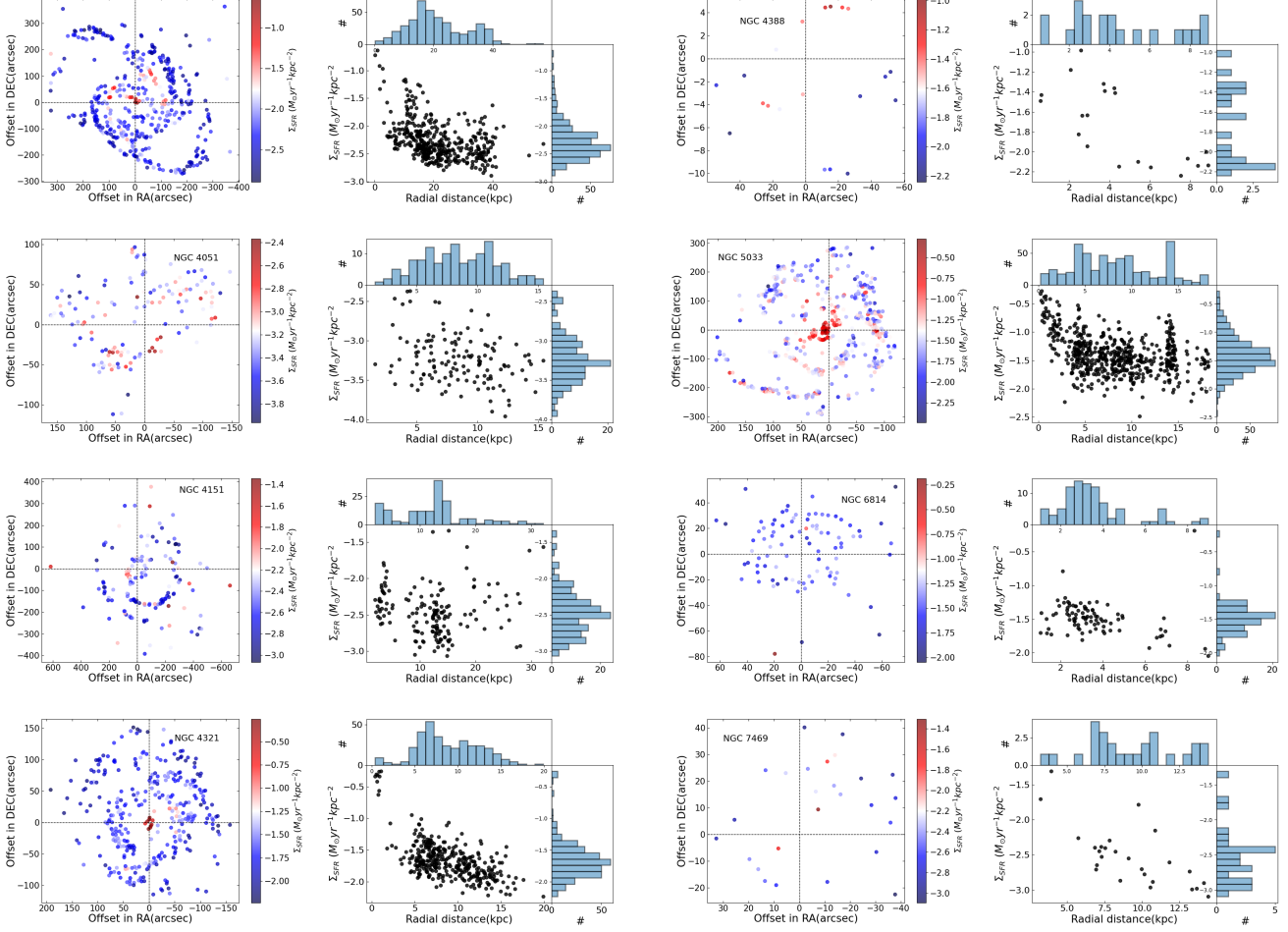


Figure 6. Spatial (left panel) and radial (right panel) variation of Σ_{SFR} in log scale.

mately 85% of the HI gas component in NGC 4388, subsequently disrupting star formation in the galaxy (Cayatte et al. 1990). Recent investigations have indicated star forming regions not coplanar with the disk, contributing to the extended outflows and suggesting recent starburst events in the spiral arms and circumnuclear region of the galaxy (Damas-Segovia et al. 2016).

We detected 20 star-forming regions in NGC 4388. These regions have FUV brightness between 22.06 mag and 15.79 mag, while in the NUV the brightness of the star forming regions varied between 22.07 mag and 15.72 mag. The areas of these regions were found to show considerable variation, spanning from 0.074 kpc^2 to 4.636 kpc^2 , with an average area of 1.268 kpc^2 and a median of 0.754 kpc^2 . The $E(B-V)$ values span a range from 0.23 mag to 0.43 mag, with an average of 0.33 mag and a median of 0.32 mag. Extinction values in the FUV band were found to have a wide range from 1.01 mag to 1.92 mag, with a mean and median of 1.46 mag and 1.43 mag, respectively, while in the NUV band, extinction varied between 0.78 mag and 1.49 mag, with a median of 1.11

mag and an average of 1.13 mag. The Σ_{SFR} within these regions in the FUV were found to vary between 5.74×10^{-3} and $103.79 \times 10^{-3} \text{ M}_{\odot} \text{ yr}^{-1} \text{ kpc}^{-2}$, with an average Σ_{SFR} of $27.23 \times 10^{-3} \text{ M}_{\odot} \text{ yr}^{-1} \text{ kpc}^{-2}$. Similarly, in the NUV band, we found Σ_{SFR} to range between 7.16×10^{-3} to $108.92 \times 10^{-3} \text{ M}_{\odot} \text{ yr}^{-1} \text{ kpc}^{-2}$. We found the average Σ_{SFR} in the NUV band of $31.38 \times 10^{-3} \text{ M}_{\odot} \text{ yr}^{-1} \text{ kpc}^{-2}$. Properties of the 564 individual star forming regions are given in Table 10.

5.6. NGC 5033

NGC 5033 is an SA(s)c-type non-barred spiral galaxy at a redshift of $z=0.00291$. It has a central bulge with a mass of approximately $2 \times 10^{10} \text{ M}_{\odot}$. It is a Seyfert 1.9 galaxy, and hosts a supermassive black hole at its center, with a mass ranging from $5-12 \times 10^6 \text{ M}_{\odot}$. It is luminous in X-rays with $L_{2-10\text{keV}} = 2.3 \times 10^{41} \text{ erg s}^{-1}$ (Terashima et al. 1999). Although high-resolution radio observations show a core-jet morphology, the radio emission from the inner disk is dominated by a starburst with the core-jet structure contributing only 7 percent

of the flux density at 1.4 GHz (Pérez-Torres & Alberdi 2007). They also report evidence of a ‘radio spur’ due to a hot bubble caused by sequential supernova explosions. The galaxy is variable in X-ray wavelengths (Papadakis et al. 2008).

The galaxy’s flat disk has a high inclination of 67.5° and shows signs of possible warping, possibly resulting from interactions or mergers. Near infrared and millimeter observations reveal a small nuclear bar, while the presence of HII regions following a ring-like pattern is evident in $H\beta$ intensity maps. A bright bar of light from the unresolved nucleus has been observed in NUV images. Radio 21cm-line studies show similarities between the HI distribution and optical characteristics, and it has been found that Σ_{SFR} is directly related to the total gas surface density. Comprehensive CO($1-0$) observations suggest that there is no starburst phenomenon in the nuclear region. Instead, star-forming regions are present in the disk region, supported by observations from the GALEX telescope. The radio and FIR luminosities of the inner regions indicate evidence of a recent short starburst in NGC 5033 (Pérez-Torres & Alberdi 2007).

We identified 557 star forming regions with a wide range of brightness. The faintest region in the FUV has a brightness of 22.51 mag, while the brightest region has a brightness of 15.43 mag. Similarly, in the NUV band, the faintest and brightest star forming regions have brightness values of 22.86 mag and 14.14 mag respectively. These star forming regions have varied sizes, ranging from 0.008 kpc^2 to 0.242 kpc^2 , with an average value of 0.020 kpc^2 . We found $E(B-V)$ to vary from 0.04 mag to 1.17 mag, with an average value of 0.51 mag and a median of 0.49 mag. Extinction values in the FUV were found to lie between 0.19 mag and 5.34 mag, with an average of 2.33 mag and a median of 1.58 mag. In the NUV band, the extinction is relatively lower, with values between 0.14 mag and 3.73 mag, with a median of 1.58 mag and an average of 1.63 mag.

The Σ_{SFR} of these star forming regions varied between 3.25×10^{-3} and $53.02 \times 10^{-2} \text{ M}_\odot \text{ yr}^{-1} \text{ kpc}^{-2}$ in FUV and between 24.81×10^{-4} and $12.78 \times 10^{-2} \text{ M}_\odot \text{ yr}^{-1} \text{ kpc}^{-2}$ in NUV. We found the Σ_{SFR} to gradually decrease radially from the centre to the outskirts, as can be seen in Fig. 6.

5.7. NGC 6814

NGC 6814 is a grand design spiral galaxy of the SAB(rs)bc type, with a face-on orientation (de Vaucouleurs et al. 1991). It is characterized by a compact bulge in both near infrared and optical wavelengths, along with a relatively weak bar extending approximately ten arcseconds in the North-South direction

(Sánchez-Portal et al. 2004; Slavcheva-Mihova & Mihov 2011). Situated at a distance of 23.22 Mpc, this galaxy hosts a type 1.5 Seyfert AGN at its center (Springob et al. 2005), with a black hole of mass $(1.85 \pm 0.35) \times 10^7 \text{ M}_\odot$ (Bentz et al. 2009). It is variable in the optical, UV, and X-ray wavelengths, with the highest variability observed in X-rays (Gallo et al. 2021; Troyer et al. 2016). It is luminous in X-rays with $L_{2-10} = 2.04 \times 10^{42} \text{ erg s}^{-1}$ (Tortosa et al. 2018). At radio frequencies, the central region appears extended in the north-south direction with a possible component towards the west, and no significant jet emission when observed with the VLA A-array, (Ulvestad & Wilson 1984; Xu et al. 1999).

Extensive work by Knapen et al. (1993) has identified numerous HII regions within the galaxy, with a comprehensive study of the luminosity functions of these regions. Interestingly, the luminosity function exhibits similar characteristics in both the outer and inner arms, offering valuable insights into the galaxy’s SF processes. In addition to HII regions, NGC 6814 displays ring-like distributions of HII, potentially featuring kinematic warping, as suggested by Liszt & Dickey (1995). Moreover, in the UV spectrum, numerous star-forming regions are evident along the spiral arms, with these arms branching into multiple fragments observable in the GALEX images (Sandage & Bedke 1994).

We identified 89 star forming regions in NGC 6814, with the faintest region at 21.21 mag and the brightest at 16.43 mag in the FUV band. These regions exhibited a range of sizes, with areas ranging from 0.029 kpc^2 to 0.422 kpc^2 , with an average area of 0.118 kpc^2 and a median area of 0.082 kpc^2 . The $E(B-V)$ values in the regions ranged from 0.15 mag to 0.59 mag, with an average of 0.43 mag. Regarding extinction in the FUV band, it was found to vary between 0.65 mag to 2.64 mag, with an average of 1.94 mag.

The Σ_{SFR} of the star forming regions identified in NGC 6814, showed variations, with the Σ_{SFR} values in the FUV band ranging from 8.96×10^{-3} to $65.25 \times 10^{-2} \text{ M}_\odot \text{ yr}^{-1} \text{ kpc}^{-2}$, with an average of $4.19 \times 10^{-2} \text{ M}_\odot \text{ yr}^{-1} \text{ kpc}^{-2}$. We found a gradual radial decrease of extinction and SFR from the centre to the outskirts of the galaxy (see Fig. 5 and Fig. 6).

5.8. NGC 7469

NGC 7469 is classified as an intermediate, nearly face-on spiral galaxy with a morphological type of (R’)SAB(rs)a (de Vaucouleurs et al. 1991). This galaxy is located at a redshift of $z=0.01627$ (Springob et al. 2005). It hosts a Seyfert 1.5 type AGN (Véron-Cetty & Véron 2006) with a black hole of mass $1.1 \times 10^7 \text{ M}_\odot$ (Peterson et al. 2014; Lu et al. 2021). It is known for

its strong X-ray emission, with a X-ray luminosity of $L_{2-10keV} = 10^{43}$ erg s $^{-1}$ (Asmus et al. 2015).

One of the prominent features of this galaxy is its circumnuclear starburst ring, situated at a distance of about 1 kiloparsec from its center. This starburst ring has been extensively observed across various wavelengths (Xu & Wang 2022). High-resolution radio continuum observations show a nucleus which is the brightest feature, and more extended emission from the circumnuclear starburst with several peaks of emission. The brightest of the compact components is a radio supernova (Colina et al. 2001). Additionally, from observations of molecular line emission at millimeter wavelengths Davies et al. (2004) suggests the presence of either a bar or a pair of spiral arms located between these ring like structures. Marquez & Moles (1994) suggest that the star forming activities in this galaxy exhibit unique characteristics, potentially influenced by its H α emission, which may be attributed to the nearby companion galaxy IC 5283.

In NGC 7469, we identified 26 star forming regions. We detected more SF regions in the northern spiral arm which may be due the effect of interaction with nearby galaxy IC 5283 as mentioned by Marquez & Moles (1994). These regions in FUV have brightness ranging between 24.47 mag and 17.67 mag. In the NUV band, the faintest star forming region is at 24.63 mag and the brightest is at 17.65 mag. Also, we found the areas of these star forming regions to vary significantly, ranging from 0.295 kpc 2 to 63.642 kpc 2 . On average, the star forming regions have an average area of 12.026 kpc 2 . The E(B–V) in these regions range from 0.06 mag to 0.64 mag. In the FUV band, we found extinction values that range from 0.27 mag to 2.68 mag, with an average of 1.17 mag. Similarly, in the NUV band, we found the extinction to vary from 0.22 mag to 2.21 mag, with a median of 0.97 mag.

The Σ_{SFR} within these star forming regions exhibits a wide range. In FUV, Σ_{SFR} varies from 8.0×10^{-4} to 49.39×10^{-3} M $_{\odot}$ yr $^{-1}$ kpc $^{-2}$, with an average of 5.72×10^{-3} M $_{\odot}$ yr $^{-1}$ kpc $^{-2}$. In NUV, we found Σ_{SFR} to vary from 7.2×10^{-4} to 77.26×10^{-3} M $_{\odot}$ yr $^{-1}$ kpc $^{-2}$, with an average Σ_{SFR} of 7.08×10^{-3} M $_{\odot}$ yr $^{-1}$ kpc $^{-2}$.

6. GLOBAL PICTURE

For the galaxies examined in this study, we observed a positive correlation between the median surface density of star formation and the extinction in the FUV band, with a Pearson correlation coefficient (r) of 0.95 and a p-value of 0.0003. This relationship is illustrated in the top panel of Fig. 7. The best-fitted line to this

correlation is given by:

$$\log\left(\frac{\Sigma_{SFR}}{M_{\odot}\text{yr}^{-1}\text{kpc}^{-2}}\right) = (0.82 \pm 0.11)A(FUV) - (3.17 \pm 0.16) \quad (5)$$

We determined the SFR using Equation 4 within the circumnuclear region, employing a 1 kpc radius aperture, and computed the total SFR using the optical R $_{25}$ aperture. In both cases, we corrected for AGN flux contamination using a 1.4'' radius aperture. Here, R $_{25}$ represents the radius at which the surface brightness reaches 25 mag per square arcsec in the optical B band. The results of these calculations are provided in Table 5. Additionally, detailed properties of each of the identified star-forming regions for all eight galaxies are presented in the Appendix.

We positioned our sources on the stellar mass versus star formation rate plane and compared their locations relative to the main sequence as described by Renzini & Peng (2015). Notably, four of our sources fell within the main sequence, one above it, and three below it. This distribution is illustrated in the bottom panel of Fig. 7. The position of the AGN in M $_{\star}$ -SFR below the main sequence has also been noticed by (Salim et al. 2007).

Furthermore, we observed a positive correlation between the star formation rate and the stellar mass. Utilizing a linear regression analysis, we determined a correlation coefficient (r) of 0.83 and a p-value of 0.02. The resulting best-fitted line is represented by the equation:

$$\log\left(\frac{SFR_{total}}{M_{\odot}\text{yr}^{-1}}\right) = (1.47 \pm 0.44) \log\left(\frac{M_{\star}}{M_{\odot}}\right) - (15.39 \pm 4.65) \quad (6)$$

We identified a modest positive correlation between the ratio of the nuclear star formation rate (SFR $_{Nuclear}$) to the total SFR (SFR $_{Total}$) and the Eddington ratio, λ_{Edd} . Here, λ_{Edd} represents the ratio of the bolometric luminosity (L $_{Bol}$) to the Eddington luminosity (L $_{Edd}$). To estimate L $_{Bol}$, we utilized the observed L $_{2-10keV}$ and applied the relation $\log(L_{Bol}) = 0.0378 \times \log(L_{2-10})^2 - 2.00 \times \log(L_{2-10}) + 60.5$ (Ichikawa et al. 2017), while L $_{Edd}$ was calculated as 1.26×10^{38} (M $_{BH}/M_{\odot}$) erg s $^{-1}$. This relationship is depicted in Fig. 8. Performing a linear least squares fit to the data points yielded a correlation coefficient (r) of 0.67 and a p-value of 0.06. The best fitted line is

$$\frac{SFR_{Nuclear}}{SFR_{Total}} = (0.05 \pm 0.02) \log(\lambda_{Edd}) + (0.31 \pm 0.05) \quad (7)$$

This correlation bears resemblance to the findings of Mountrichas & Buat (2023) regarding the relationship between SFR and λ_{Edd} . However, we noted that

Table 4. Summary of the identified star forming regions for all sources. The values of Σ_{SFR} are in units of $10^{-3} M_{\odot} \text{ yr}^{-1} \text{ kpc}^{-2}$.

Name	N	area (kpc ²)	E(B-V)	Mean		Σ_{SFR}^{FUV}	Σ_{SFR}^{NUV}	area (kpc ²)	E(B-V)	Median		Σ_{SFR}^{FUV}	Σ_{SFR}^{NUV}
				A_{FUV} (mag)	A_{NUV} (mag)					A_{FUV} (mag)	A_{NUV} (mag)		
NGC 1365	418	0.713	0.212	0.93	0.68	8.90	11.19	0.215	0.195	0.86	0.63	4.65	4.83
NGC 4051	131	0.341	-0.046	-0.19	-0.17	0.77	0.70	0.207	-0.038	-0.16	-0.14	0.54	0.48
NGC 4151	161	0.187	0.252	1.13	0.94	4.84	5.71	0.027	0.227	1.02	0.84	3.32	3.56
NGC 4321	340	0.159	0.356	1.62	--	34.37	--	0.116	0.36	1.60	--	20.02	--
NGC 4388	20	1.268	0.325	1.46	1.13	27.23	31.38	0.755	0.318	1.43	1.11	19.04	23.05
NGC 5033	557	0.021	0.509	2.33	1.63	57.73	128.34	0.013	0.494	2.26	1.58	37.75	62.33
NGC 6814	89	0.120	0.432	1.94	--	41.96	--	0.083	0.452	2.03	--	32.95	--
NGC 7469	26	12.026	0.277	1.17	0.96	5.71	7.08	4.973	0.277	1.17	0.97	2.66	2.88

this correlation is heavily influenced by two points, NGC 7469 and NGC 4051. Thus, further observations with more sources are required to confirm this correlation robustly. Nevertheless, the observed correlation suggests that AGN activity (jet and/or radiation) positively influences the star formation characteristics near the nuclear region, with minimal impact observed at greater distances from the nuclear region. However, disentangling the contribution of AGN jet and radiation is not possible using only the observations reported in this paper. Our observation aligns with both simulations (Bollati et al. 2023) and observational studies (Lammers et al. 2023), which support the operation of feedback processes primarily within the central kilo-parsec region in AGN host galaxies.

7. SUMMARY

We carried out an investigation of the SF characteristics of galaxies hosting AGN using observations carried out in UV. Our sample consists of seven Seyfert and one LINER type AGN. Our approach involved the identification of star-forming regions, carrying out aperture photometry of the identified star-forming regions, correcting the derived brightness for both Milky Way and internal extinction, estimation of SFR and the correlation of SFR with various derived parameters. The findings of this work are summarized below.

1. We identified many star-forming regions for all eight galaxies hosting AGN. For NGC 5033, we detected the maximum number of SF regions. Most of the identified star-forming regions have sizes in excess of 30 parsecs, with areas ranging between 0.010 and 63.642 kpc².
2. The extinction corrected SFR of the star-forming regions considering all the sources studied in this work are found to range between $1.09 \times 10^{-4} M_{\odot} \text{ yr}^{-1}$ and $22.96 \times 10^{-2} M_{\odot} \text{ yr}^{-1}$ in FUV, while in NUV it varies between 8.15×10^{-5} and $6.634 M_{\odot} \text{ yr}^{-1}$. We found the Σ_{SFR} in NUV to be larger than that at FUV, though the median values are found to be similar.

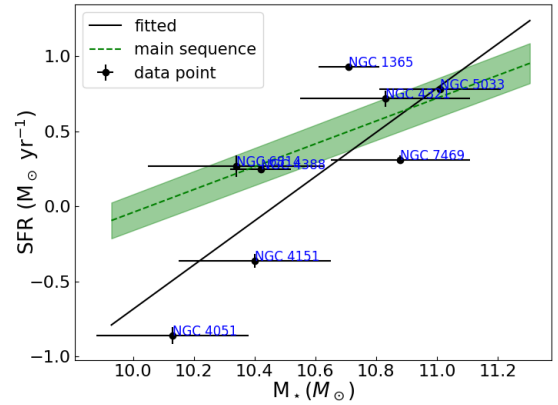
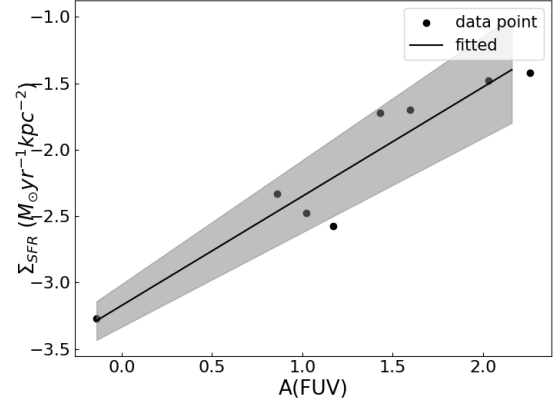


Figure 7. Top panel: Variation of median Σ_{SFR} against median extinction in FUV of SF regions for the sources studied in this work. Bottom panel: Variation of SFR with stellar mass. The dotted line is the MS of SF from Renzini & Peng 2015, and the solid line is the best-fitted linear regression line.

3. We detected two outer spiral arms for NGC 4151 in both FUV and NUV bands. These spiral arms are much extended beyond R25 aperture.
4. For five galaxies, NGC 1365, NGC 4051, NGC 4321, NGC 5033 and NGC 6814, we found both the internal extinction and the Σ_{SFR} to gradually decrease from the centre towards the outer

Table 5. The properties of the galaxies in FUV. The units of SFR are in $M_{\odot} \text{ yr}^{-1}$, while that of Σ_{SFR} are in units of $10^{-3} M_{\odot} \text{ yr}^{-1} \text{ kpc}^{-2}$.

Name	SFR_{Total}	$SFR_{Nuclear}$	Σ_{SFR}^{Total}	$\Sigma_{SFR}^{Nuclear}$
NGC 1365	8.469 ± 0.128	1.192 ± 0.019	2.83 ± 0.04	94.82 ± 1.62
NGC 4051	0.138 ± 0.008	0.050 ± 0.003	1.40 ± 0.08	15.82 ± 0.9
NGC 4151	0.434 ± 0.019	0.102 ± 0.004	1.48 ± 0.07	8.12 ± 0.41
NGC 4321	5.210 ± 0.281	0.617 ± 0.033	3.72 ± 0.21	48.11 ± 2.60
NGC 4388	0.32 ± 0.005	1.77 ± 0.02	3.22 ± 0.04	25.57 ± 0.4
NGC 5033	6.058 ± 0.0997	1.116 ± 0.024	10.34 ± 0.20	88.78 ± 1.91
NGC 6814	1.859 ± 0.134	0.351 ± 0.025	7.25 ± 0.52	27.90 ± 2.00
NGC 7469	2.042 ± 0.057	0.792 ± 0.030	4.25 ± 0.14	63.00 ± 2.41

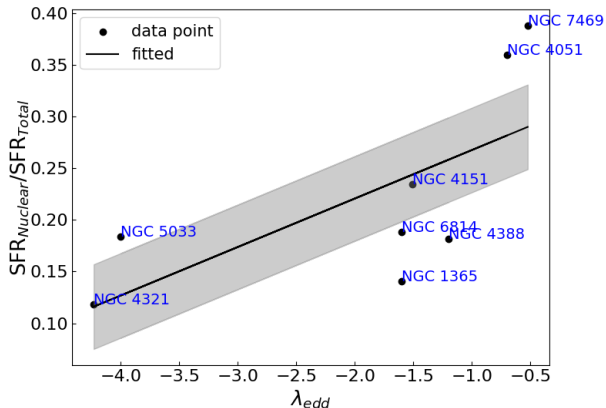


Figure 8. Variation of the ratio of $SFR_{Nuclear}$ to SFR_{Total} with λ_{Edd} . The solid line is the linear least squares fit to the data and the shaded region is 95% confidence region.

regions, while this was not significant in the other sources.

5. We found a positive correlation between the median Σ_{SFR} and the median extinction in FUV for the star-forming regions.
6. Among the observed sources, four are situated within the main sequence (MS) of star-forming galaxies; while the remaining four are positioned away from the MS.
7. All sources display a positive correlation between SFR and M_* , with a slope that is notably steeper than MS.

8. We found the SFR in the nuclear region dominant over the total SFR.

9. The ratio of $SFR_{Nuclear}$ to SFR_{Total} exhibits a weak positive correlation with λ_{Edd} . This correlation points to the influence of AGN on enhancing the SF characteristics of the hosts and the impact being dominant in the central region with no effect on scales beyond the nuclear region probed in this work.

ACKNOWLEDGMENTS

This manuscript uses the data from the AstroSat mission of the Indian Space Research Organization (ISRO), archived at the Indian Space Science Data Center (ISSDC). This manuscript uses UVIT data processed by the payload operations centre at IIA. The UVIT is built in collaboration between IIA, IUCAA, TIFR, ISRO, and CSA. We have used the NASA-NED database. PN thanks the Council of Scientific and Industrial Research (CSIR), Government of India, for supporting her research under the CSIR Junior/Senior Research Fellowship program through grant no. 09/079(2867)/2021-EMR-I. PD wants to thank the Board of Graduate Studies, Indian Institute of Astrophysics, for their support through the Visiting student program.

Facilities: UVIT(Astrosat)

Software: IRAF (Tody 1986), SExtractor (Bertin & Arnouts 1996), Photutils (Bradley et al. 2020)

APPENDIX

A. SOME EXTRA MATERIAL

Table 6. Properties of the identified star forming regions for NGC 1365. Here, a,b, θ are the semi-major axis, semi-minor axis and the position angle of the star forming regions, area is the area of the regions in kpc², E(B−V) is the colour excess in magnitude, m_{FUV} and m_{NUV} are the magnitudes in FUV and NUV bands, A_{FUV} and A_{NUV} are the extinction in FUV and NUV bands, and Σ_{FUV} and Σ_{NUV} are the surface density of SFR in units of $10^{-3} M_{\odot} \text{ yr}^{-1} \text{ kpc}^{-2}$ in FUV and NUV bands respectively. Only the first 10 entries are given, and the table in full is available in the electronic version of the article.

RA	DEC	a	b	θ	r_d	area	E(B−V)	m_{FUV}	m_{NUV}	A_{FUV}	A_{NUV}	Σ_{FUV}	Σ_{NUV}
03:33:26.07	-36:12:49.39	5.58	3.45	0.009	36.26	0.936	0.102	17.97±0.08	18.18±0.07	0.44	0.33	13.82±0.46	12.0±0.32
03:33:26.09	-36:12:44.44	5.16	2.59	0.769	35.69	0.651	0.109	18.55±0.1	18.74±0.08	0.48	0.35	11.75±0.49	10.32±0.35
03:33:26.02	-36:12:54.31	2.65	2.13	1.504	36.84	0.275	0.112	19.57±0.16	19.76±0.13	0.49	0.36	10.8±0.7	9.54±0.51
03:33:25.51	-36:12:41.75	3.76	1.66	0.79	35.79	0.303	0.088	19.73±0.17	19.95±0.14	0.38	0.28	8.5±0.57	7.24±0.4
03:33:24.70	-36:12:53.92	4.03	2.49	0.291	37.7	0.489	0.091	19.39±0.14	19.61±0.12	0.4	0.29	7.16±0.42	6.12±0.3
03:33:24.81	-36:12:50.19	3.12	2.23	-0.497	37.21	0.338	0.102	19.77±0.17	19.98±0.14	0.45	0.33	7.3±0.51	6.34±0.36
03:33:25.11	-36:12:43.54	4.24	2.51	0.774	36.27	0.519	0.111	19.5±0.16	19.68±0.13	0.49	0.36	6.15±0.38	5.42±0.28
03:33:24.33	-36:12:58.13	4.89	2.59	-0.051	38.42	0.614	0.097	19.84±0.18	20.05±0.15	0.42	0.31	3.79±0.27	3.27±0.19
03:33:23.91	-36:12:55.71	3.86	2.11	-1.316	38.46	0.396	0.118	20.43±0.24	20.61±0.2	0.52	0.38	3.39±0.32	3.02±0.24
03:33:27.23	-36:12:48.16	6.02	4.37	0.492	35.39	1.278	0.183	19.32±0.16	19.39±0.13	0.8	0.59	2.94±0.18	2.89±0.15

Table 7. Same as Table 6, but for NGC 4051

RA	DEC	a	b	θ	r_d	area	E(B−V)	m_{FUV}	m_{NUV}	A_{FUV}	A_{NUV}	Σ_{FUV}	Σ_{NUV}
12:03:09.64	44:33:19.98	1.87	1.17	0.809	10.86	0.106	-0.11	22.32±0.95	22.56±0.83	-0.46	-0.41	0.25±0.09	0.21±0.07
12:03:11.02	44:33:26.68	2.33	1.65	0.563	11.84	0.187	-0.034	20.09±0.41	20.28±0.36	-0.14	-0.12	1.09±0.18	0.96±0.14
12:03:11.04	44:33:22.87	2.81	1.68	0.024	11.38	0.23	-0.068	20.04±0.38	20.26±0.33	-0.29	-0.25	0.92±0.14	0.8±0.11
12:03:10.37	44:33:19.07	1.92	1.14	0.224	10.8	0.106	-0.162	21.74±0.67	22.02±0.59	-0.68	-0.6	0.42±0.11	0.34±0.08
12:03:10.51	44:33:17.01	2.12	1.51	0.801	10.56	0.156	-0.189	21.5±0.58	21.8±0.51	-0.8	-0.7	0.36±0.08	0.28±0.06
12:03:10.72	44:33:29.44	2.69	1.48	0.945	12.13	0.193	-0.144	21.73±0.69	22.0±0.61	-0.61	-0.54	0.23±0.06	0.19±0.05
12:03:09.50	44:33:13.86	1.86	1.13	1.502	10.1	0.102	0.016	21.35±0.76	21.51±0.67	0.07	0.06	0.62±0.19	0.57±0.15
12:03:06.61	44:33:08.27	2.08	1.73	0.683	10.21	0.175	-0.153	20.92±0.48	21.19±0.42	-0.65	-0.57	0.54±0.1	0.44±0.07
12:02:59.81	44:32:58.57	1.17	0.88	0.877	15.4	0.05	0.006	22.25±1.12	22.41±0.98	0.03	0.02	0.56±0.25	0.5±0.2
12:03:03.06	44:33:00.84	1.34	1.1	1.289	12.16	0.072	-0.038	21.99±0.93	22.18±0.81	-0.16	-0.14	0.49±0.18	0.43±0.14

Table 8. Same as Table 6, but for NGC 4151

RA	DEC	a	b	θ	r_d	area	E(B−V)	m_{FUV}	m_{NUV}	A_{FUV}	A_{NUV}	Σ_{FUV}	Σ_{NUV}
12:10:25.98	39:30:37.96	1.3	1.08	0.033	23.94	0.017	0.555	21.35±0.67	21.01±0.57	2.49	2.06	8.48±2.28	12.11±2.78
12:10:15.56	39:28:28.52	1.85	1.32	0.824	19.69	0.03	0.199	21.66±0.45	21.7±0.4	0.89	0.74	3.62±0.66	3.69±0.58
12:09:48.51	39:23:03.25	2.0	1.89	-1.56	32.17	0.046	0.673	19.01±0.29	18.55±0.25	3.01	2.5	27.07±3.18	43.26±4.29
12:09:59.41	39:24:23.45	1.64	1.27	0.176	23.93	0.025	0.342	21.8±0.6	21.69±0.52	1.53	1.27	3.75±0.89	4.38±0.9
12:10:26.60	39:29:08.51	1.36	1.09	1.256	18.4	0.018	0.435	20.01±0.31	19.8±0.27	1.95	1.61	27.32±3.44	34.8±3.75
12:10:02.62	39:24:44.85	1.94	1.45	0.415	21.66	0.034	0.4742	1.21±0.56	20.95±0.48	2.12	1.76	4.77±1.06	6.31±1.21
12:10:14.92	39:26:39.12	1.2	1.05	0.15	15.36	0.015	0.151	22.51±0.62	22.59±0.54	0.68	0.56	3.22±0.8	3.14±0.68
12:10:12.89	39:26:11.72	1.85	1.16	-0.093	15.78	0.026	0.222	23.0±0.85	23.0±0.74	1.0	0.82	1.21±0.41	1.26±0.38
12:10:21.88	39:27:49.60	1.96	0.95	1.291	15.1	0.023	0.432	21.79±0.68	21.58±0.58	1.94	1.6	4.23±1.15	5.37±1.26
12:10:20.80	39:27:28.18	1.38	1.18	-0.499	14.41	0.02	0.187	23.03±0.82	23.07±0.72	0.84	0.69	1.54±0.51	1.55±0.44

Table 9. Same as Table 6, but for NGC 4321

RA	DEC	a	b	θ	r_d	area	E(B−V)	m_{FUV}	m_{NUV}	A_{FUV}	A_{NUV}	Σ_{FUV}	Σ_{NUV}
12:22:57.31	15:51:46.07	3.24	2.8	0.295	15.53	0.307	0.226	18.12±0.31	–	1.01	–	25.57±3.21	–
12:22:56.97	15:51:51.84	2.51	1.43	1.052	16.01	0.121	0.244	20.65±0.56	–	1.09	–	6.32±1.42	–
12:22:58.48	15:51:36.93	1.85	1.26	-1.37	15.13	0.079	0.351	19.86±0.53	–	1.57	–	19.87±4.2	–
12:22:59.49	15:51:27.17	1.88	1.53	1.296	14.82	0.097	0.219	19.63±0.42	–	0.98	–	20.08±3.39	–
12:22:56.51	15:51:42.52	4.41	2.56	0.383	14.94	0.382	0.235	18.5±0.34	–	1.05	–	14.53±1.98	–
12:22:56.12	15:51:46.23	2.35	1.2	-1.522	15.24	0.095	0.273	20.43±0.48	–	1.22	–	9.82±1.9	–
12:22:56.42	15:51:48.90	1.75	1.25	1.463	15.57	0.074	0.225	21.18±0.52	–	1.01	–	6.33±1.32	–
12:22:55.10	15:51:44.64	2.84	1.4	0.688	14.97	0.134	0.255	20.42±0.6	–	1.14	–	7.01±1.68	–
12:23:04.49	15:50:59.37	1.55	1.33	-1.017	17.61	0.069	0.244	20.68±0.69	–	1.09	–	10.66±2.93	–
12:22:53.03	15:51:48.46	2.72	2.12	1.216	15.63	0.195	0.179	18.25±0.3	–	0.8	–	35.83±4.24	–

REFERENCES

- Agrawal, P. C. 2006, *Advances in Space Research*, 38, 2989, doi: 10.1016/j.asr.2006.03.038
- Allison, J. R., Sadler, E. M., & Meekin, A. M. 2014, *MNRAS*, 440, 696, doi: 10.1093/mnras/stu289

Table 10. Same as Table 6, but for NGC 4388

RA	DEC	a	b	θ	r_d	area	E(B-V)	m_{FUV}	m_{NUV}	A_{FUV}	A_{NUV}	Σ_{FUV}	Σ_{NUV}
12:25:43.27	12:39:42.04	0.92	0.92	-0.954	8.39	0.074	0.225	22.06±0.68	22.07±0.52	1.01	0.78	7.23±1.96	7.54±1.55
12:25:43.48	12:39:41.62	2.42	2.04	-0.846	7.87	0.428	0.272	19.97±0.28	19.91±0.21	1.22	0.95	8.56±0.97	9.48±0.81
12:25:43.07	12:39:39.56	1.64	1.28	0.735	8.9	0.182	0.314	21.07±0.51	20.96±0.38	1.41	1.09	7.31±1.48	8.53±1.29
12:25:45.71	12:39:47.73	1.05	0.95	-0.672	2.58	0.086	0.23	19.0±0.17	19.0±0.13	1.03	0.8	103.79±7.08	108.92±5.65
12:25:45.92	12:39:47.65	4.78	2.05	-0.224	2.08	0.848	0.244	17.01±0.08	16.99±0.06	1.09	0.85	66.08±2.04	70.63±1.68
12:25:45.23	12:39:47.65	2.5	1.72	-0.465	3.7	0.372	0.285	18.25±0.14	18.17±0.1	1.27	0.99	48.23±2.6	54.22±2.22
12:25:44.99	12:39:47.55	3.87	3.55	0.915	4.28	1.187	0.304	17.22±0.09	17.11±0.07	1.36	1.06	39.06±1.42	44.97±1.24
12:25:46.85	12:39:46.42	11.45	4.69	0.223	0.62	4.636	0.277	15.79±0.06	15.72±0.04	1.24	0.96	37.23±0.82	41.47±0.7
12:25:48.46	12:39:39.30	1.93	1.46	0.343	4.25	0.243	0.374	18.82±0.2	18.62±0.15	1.68	1.3	43.59±3.54	54.84±3.32
12:25:48.25	12:39:39.08	2.99	2.38	-1.213	3.76	0.616	0.365	17.88±0.13	17.69±0.1	1.64	1.27	40.89±2.16	50.83±2.01

Table 11. Same as table 6, but for NGC 5033

RA	DEC	a	b	θ	r_d	area	E(B-V)	m_{FUV}	m_{NUV}	A_{FUV}	A_{NUV}	Σ_{FUV}	Σ_{NUV}
13:13:29.99	36:30:47.06	1.41	1.19	1.404	18.2	0.02	0.416	19.95±0.72	19.61±0.6	1.91	1.33	25.6±7.35	36.81±8.84
13:13:28.32	36:30:45.54	0.92	0.92	0.394	18.21	0.01	0.348	20.74±0.95	20.52±0.81	1.59	1.11	24.14±9.15	30.88±10.02
13:13:28.43	36:30:46.39	0.92	0.92	1.229	18.16	0.01	0.321	20.52±0.83	20.35±0.71	1.47	1.03	29.75±9.84	36.38±10.39
13:13:28.80	36:30:51.67	0.92	0.92	1.469	17.85	0.01	0.403	20.58±0.94	20.26±0.79	1.85	1.29	27.99±10.54	39.35±12.46
13:13:28.53	36:30:57.64	1.55	0.86	0.926	17.47	0.016	0.406	20.14±0.77	19.81±0.65	1.86	1.3	27.23±8.38	38.46±9.94
13:13:28.58	36:30:51.86	0.92	0.92	1.295	17.83	0.01	0.381	20.48±0.87	20.2±0.74	1.75	1.22	30.82±10.77	41.77±12.36
13:13:28.43	36:30:51.28	0.92	0.92	1.306	17.86	0.01	0.363	20.81±0.99	20.56±0.85	1.66	1.16	22.77±9.05	29.92±10.13
13:13:28.34	36:30:49.68	0.92	0.92	1.433	17.95	0.01	0.594	19.98±0.93	19.31±0.73	2.72	1.9	48.51±17.97	94.33±27.39
13:13:28.65	36:30:49.22	0.92	0.92	-1.35	17.99	0.01	0.575	20.03±0.92	19.39±0.73	2.64	1.84	46.5±17.14	87.66±25.5
13:13:28.16	36:31:05.42	1.78	0.94	-0.921	16.97	0.02	0.436	19.67±0.64	19.29±0.54	2.0	1.4	33.27±8.59	49.49±10.62

Table 12. Same as Table 6, but for NGC 6814

RA	DEC	a	b	θ	r_d	area	E(B-V)	m_{FUV}	m_{NUV}	A_{FUV}	A_{NUV}	Σ_{FUV}	Σ_{NUV}
19:42:41.88	-10:20:43.08	1.37	1.23	0.738	8.32	0.057	0.389	16.43±0.21	-	1.74	-	652.5±54.85	-
19:42:40.54	-10:20:33.98	1.68	1.05	0.28	7.14	0.06	0.224	20.65±0.43	-	1.0	-	12.75±2.2	-
19:42:36.72	-10:20:28.14	1.3	0.91	-1.042	8.82	0.04	0.229	21.21±0.52	-	1.03	-	11.53±2.39	-
19:42:37.13	-10:20:06.59	1.22	0.84	-0.395	6.81	0.035	0.296	20.88±0.5	-	1.32	-	17.91±3.55	-
19:42:38.23	-10:19:57.19	1.29	0.92	0.336	4.91	0.04	0.435	19.97±0.46	-	1.95	-	35.56±6.61	-
19:42:41.95	-10:19:50.36	1.67	0.8	-0.444	3.35	0.045	0.455	19.36±0.35	-	2.04	-	55.47±7.82	-
19:42:41.98	-10:19:45.70	2.11	1.02	-1.221	3.02	0.073	0.436	19.98±0.4	-	1.96	-	19.46±3.11	-
19:42:41.74	-10:19:48.66	6.32	1.98	-0.635	3.01	0.422	0.475	18.31±0.39	-	2.13	-	15.57±2.45	-
19:42:43.52	-10:19:44.90	1.15	0.99	0.815	4.93	0.038	0.411	20.09±0.45	-	1.84	-	33.15±5.94	-
19:42:40.17	-10:19:42.61	1.66	1.39	-0.277	1.92	0.078	0.472	18.88±0.35	-	2.12	-	49.8±6.9	-

Table 13. Same as Table 6, but for NGC 7469

RA	DEC	a	b	θ	r_d	area	E(B-V)	m_{FUV}	m_{NUV}	A_{FUV}	A_{NUV}	Σ_{FUV}	Σ_{NUV}
23:03:13.11	08:52:03.81	0.92	0.92	-1.32	14.41	0.295	0.064	24.46±2.14	24.63±1.66	0.27	0.22	0.8±0.69	0.72±0.48
23:03:16.17	08:52:21.09	4.14	2.3	-1.159	3.22	3.278	0.184	18.37±0.18	18.41±0.14	0.78	0.64	19.83±1.45	19.98±1.15
23:03:15.13	08:52:35.74	1.68	1.49	-0.205	3.93	0.859	0.635	18.83±0.48	18.4±0.37	2.68	2.21	49.39±9.51	77.26±11.41
23:03:14.89	08:52:53.73	2.66	1.67	-1.165	9.75	1.525	0.238	19.4±0.3	19.39±0.23	1.0	0.83	16.49±1.98	17.5±1.63
23:03:14.69	08:52:56.15	3.13	1.61	-0.675	10.87	1.736	0.175	20.17±0.38	20.22±0.29	0.74	0.61	7.11±1.07	7.1±0.83
23:03:16.93	08:52:17.07	12.04	4.8	1.246	7.13	19.877	0.327	18.27±0.22	18.16±0.17	1.38	1.14	3.57±0.31	4.13±0.28
23:03:15.19	08:52:42.47	2.47	1.49	0.5	5.73	1.27	0.279	20.79±0.6	20.73±0.46	1.18	0.97	5.51±1.32	6.09±1.12
23:03:14.71	08:52:44.67	5.81	2.37	1.389	7.52	4.735	0.275	19.72±0.37	19.66±0.28	1.16	0.96	3.97±0.58	4.37±0.5
23:03:15.98	08:52:49.40	2.07	1.58	-0.847	7.83	1.126	0.292	21.0±0.68	20.93±0.52	1.24	1.02	5.1±1.38	5.71±1.19
23:03:16.51	08:52:50.48	7.9	6.08	0.404	9.09	16.523	0.216	18.73±0.22	18.74±0.17	0.91	0.75	2.82±0.25	2.94±0.2

Álvarez-Álvarez, M., Díaz, A. I., Terlevich, E., & Terlevich, R. 2015, MNRAS, 451, 3173, doi: [10.1093/mnras/stv1123](https://doi.org/10.1093/mnras/stv1123)
 Andreani, P., Boselli, A., Ciesla, L., et al. 2018, A&A, 617, A33, doi: [10.1051/0004-6361/201832873](https://doi.org/10.1051/0004-6361/201832873)
 Arsenault, R. 1989, A&A, 217, 66
 Asmus, D., Gandhi, P., Hönig, S. F., Smette, A., & Duschl, W. J. 2015, MNRAS, 454, 766, doi: [10.1093/mnras/stv1950](https://doi.org/10.1093/mnras/stv1950)

Bentz, M. C., & Manne-Nicholas, E. 2018, ApJ, 864, 146, doi: [10.3847/1538-4357/aad808](https://doi.org/10.3847/1538-4357/aad808)
 Bentz, M. C., Denney, K. D., Cackett, E. M., et al. 2006, ApJ, 651, 775, doi: [10.1086/507417](https://doi.org/10.1086/507417)
 Bentz, M. C., Walsh, J. L., Barth, A. J., et al. 2009, ApJ, 705, 199, doi: [10.1088/0004-637X/705/1/199](https://doi.org/10.1088/0004-637X/705/1/199)
 Bertin, E., & Arnouts, S. 1996, A&AS, 117, 393, doi: [10.1051/aas:1996164](https://doi.org/10.1051/aas:1996164)

- Bing, L., Shi, Y., Chen, Y., et al. 2019, *MNRAS*, 482, 194, doi: [10.1093/mnras/sty2662](https://doi.org/10.1093/mnras/sty2662)
- Bollati, F., Lupi, A., Dotti, M., & Haardt, F. 2023, arXiv e-prints, arXiv:2311.07576, doi: [10.48550/arXiv.2311.07576](https://doi.org/10.48550/arXiv.2311.07576)
- Bosma, A., Ekers, R. D., & Lequeux, J. 1977, *A&A*, 57, 97
- Bradley, L., Sipőcz, B., Robitaille, T., et al. 2020, *astropy/photutils: 1.0.0*, Zenodo, doi: [10.5281/zenodo.4044744](https://doi.org/10.5281/zenodo.4044744)
- Brenneman, L. W., Risaliti, G., Elvis, M., & Nardini, E. 2013, *MNRAS*, 429, 2662, doi: [10.1093/mnras/sts555](https://doi.org/10.1093/mnras/sts555)
- Byrne, L., Faucher-Giguère, C.-A., Wellons, S., et al. 2023, arXiv e-prints, arXiv:2310.16086, doi: [10.48550/arXiv.2310.16086](https://doi.org/10.48550/arXiv.2310.16086)
- Calzetti, D., Armus, L., Bohlin, R. C., et al. 2000, *ApJ*, 533, 682, doi: [10.1086/308692](https://doi.org/10.1086/308692)
- Cardelli, J. A., Clayton, G. C., & Mathis, J. S. 1989, *ApJ*, 345, 245, doi: [10.1086/167900](https://doi.org/10.1086/167900)
- Cayette, V., van Gorkom, J. H., Balkowski, C., & Kotanyi, C. 1990, *AJ*, 100, 604, doi: [10.1086/115545](https://doi.org/10.1086/115545)
- Cid Fernandes, R., Gu, Q., Melnick, J., et al. 2004, *MNRAS*, 355, 273, doi: [10.1111/j.1365-2966.2004.08321.x](https://doi.org/10.1111/j.1365-2966.2004.08321.x)
- Colina, L., Alberdi, A., Torrelles, J. M., Panagia, N., & Wilson, A. S. 2001, *ApJL*, 553, L19, doi: [10.1086/320507](https://doi.org/10.1086/320507)
- Couto, G. S., & Storchi-Bergmann, T. 2023, *Galaxies*, 11, 47, doi: [10.3390/galaxies11020047](https://doi.org/10.3390/galaxies11020047)
- Damas-Segovia, A., Beck, R., Vollmer, B., et al. 2016, *ApJ*, 824, 30, doi: [10.3847/0004-637X/824/1/30](https://doi.org/10.3847/0004-637X/824/1/30)
- Davies, R. I., Müller Sánchez, F., Genzel, R., et al. 2007, *ApJ*, 671, 1388, doi: [10.1086/523032](https://doi.org/10.1086/523032)
- Davies, R. I., Sugai, H., & Ward, M. J. 1998, *MNRAS*, 300, 388, doi: [10.1046/j.1365-8711.1998.01928.x](https://doi.org/10.1046/j.1365-8711.1998.01928.x)
- Davies, R. I., Tacconi, L. J., & Genzel, R. 2004, *The Astrophysical Journal*, 602, 148, doi: [10.1086/380995](https://doi.org/10.1086/380995)
- de Vaucouleurs, G., de Vaucouleurs, A., Corwin, Herold G., J., et al. 1991, *Third Reference Catalogue of Bright Galaxies*
- Diniz, M. R., Riffel, R. A., Storchi-Bergmann, T., & Riffel, R. 2019, *MNRAS*, 487, 3958, doi: [10.1093/mnras/stz1329](https://doi.org/10.1093/mnras/stz1329)
- Evans, I. N., Koratkar, A. P., Storchi-Bergmann, T., et al. 1996, *ApJS*, 105, 93, doi: [10.1086/192308](https://doi.org/10.1086/192308)
- Falcke, H., Wilson, A. S., & Simpson, C. 1998, *ApJ*, 502, 199, doi: [10.1086/305886](https://doi.org/10.1086/305886)
- Ferrarese, L., & Merritt, D. 2000, *ApJL*, 539, L9, doi: [10.1086/312838](https://doi.org/10.1086/312838)
- Ferreras, I., Cropper, M., Kawata, D., Page, M., & Hoversten, E. A. 2012, *MNRAS*, 424, 1636, doi: [10.1111/j.1365-2966.2012.21017.x](https://doi.org/10.1111/j.1365-2966.2012.21017.x)
- Fiore, F., Feruglio, C., Shankar, F., et al. 2017, *A&A*, 601, A143, doi: [10.1051/0004-6361/201629478](https://doi.org/10.1051/0004-6361/201629478)
- Forster, K., Leighly, K. M., & Kay, L. E. 1999, *ApJ*, 523, 521, doi: [10.1086/307761](https://doi.org/10.1086/307761)
- Gaia Collaboration, Vallenari, A., Brown, A. G. A., et al. 2022, arXiv e-prints, arXiv:2208.00211, <https://arxiv.org/abs/2208.00211>
- Gallagher, R., Maiolino, R., Belfiore, F., et al. 2019, *MNRAS*, 485, 3409, doi: [10.1093/mnras/stz564](https://doi.org/10.1093/mnras/stz564)
- Gallo, L. C., Gonzalez, A. G., & Miller, J. M. 2021, *ApJL*, 908, L33, doi: [10.3847/2041-8213/abdcb5](https://doi.org/10.3847/2041-8213/abdcb5)
- García-Bernete, I., Alonso-Herrero, A., García-Burillo, S., et al. 2021, *A&A*, 645, A21, doi: [10.1051/0004-6361/202038256](https://doi.org/10.1051/0004-6361/202038256)
- García-Burillo, S., Sempere, M. J., Combes, F., & Neri, R. 1998, *A&A*, 333, 864, <https://arxiv.org/abs/astro-ph/9803006>
- García-González, J., Alonso-Herrero, A., Hernán-Caballero, A., et al. 2016, *MNRAS*, 458, 4512, doi: [10.1093/mnras/stw626](https://doi.org/10.1093/mnras/stw626)
- Gebhardt, K., Bender, R., Bower, G., et al. 2000, *ApJL*, 539, L13, doi: [10.1086/312840](https://doi.org/10.1086/312840)
- Georgiev, I. Y., Böker, T., Leigh, N., Lützgendorf, N., & Neumayer, N. 2016, *MNRAS*, 457, 2122, doi: [10.1093/mnras/stw093](https://doi.org/10.1093/mnras/stw093)
- Ghosh, S. K., Tandon, S. N., Singh, S. K., et al. 2022, *Journal of Astrophysics and Astronomy*, 43, 77, doi: [10.1007/s12036-022-09842-7](https://doi.org/10.1007/s12036-022-09842-7)
- González-Martín, O., Masegosa, J., Márquez, I., Guainazzi, M., & Jiménez-Bailón, E. 2009, *A&A*, 506, 1107, doi: [10.1051/0004-6361/200912288](https://doi.org/10.1051/0004-6361/200912288)
- Gu, Q., Dultzin-Hacyan, D., & de Diego, J. A. 2001, *RMxAA*, 37, 3, doi: [10.48550/arXiv.astro-ph/0011419](https://doi.org/10.48550/arXiv.astro-ph/0011419)
- Häring, N., & Rix, H.-W. 2004, *ApJL*, 604, L89, doi: [10.1086/383567](https://doi.org/10.1086/383567)
- Harrison, C. M. 2017, *Nature Astronomy*, 1, 0165, doi: [10.1038/s41550-017-0165](https://doi.org/10.1038/s41550-017-0165)
- Hennig, M. G., Riffel, R. A., Dors, O. L., et al. 2018, *MNRAS*, 477, 1086, doi: [10.1093/mnras/sty547](https://doi.org/10.1093/mnras/sty547)
- Hervella Seoane, K., Ramos Almeida, C., Acosta Pulido, J. A., et al. 2023, arXiv e-prints, arXiv:2309.10572, doi: [10.48550/arXiv.2309.10572](https://doi.org/10.48550/arXiv.2309.10572)
- Hummel, E., & Saikia, D. J. 1991, *A&A*, 249, 43
- Ichikawa, K., Ricci, C., Ueda, Y., et al. 2017, *ApJ*, 835, 74, doi: [10.3847/1538-4357/835/1/74](https://doi.org/10.3847/1538-4357/835/1/74)
- Immler, S., Pietsch, W., & Aschenbach, B. 1998, *A&A*, 331, 601
- Jones, S., McHardy, I., Moss, D., et al. 2011, *MNRAS*, 412, 2641, doi: [10.1111/j.1365-2966.2010.18105.x](https://doi.org/10.1111/j.1365-2966.2010.18105.x)
- Jones, S., McHardy, I., Moss, D., et al. 2011, *Monthly Notices of the Royal Astronomical Society*, 412, 2641, doi: [10.1111/j.1365-2966.2010.18105.x](https://doi.org/10.1111/j.1365-2966.2010.18105.x)

- Kennicutt, R. C., & Evans, N. J. 2012, *ARA&A*, 50, 531, doi: [10.1146/annurev-astro-081811-125610](https://doi.org/10.1146/annurev-astro-081811-125610)
- Khachikian, E. Y., & Weedman, D. W. 1974, *ApJ*, 192, 581, doi: [10.1086/153093](https://doi.org/10.1086/153093)
- Knapen, J. H., Arnth-Jensen, N., Cepa, J., & Beckman, J. E. 1993, *AJ*, 106, 56, doi: [10.1086/116620](https://doi.org/10.1086/116620)
- Kumari, N., Jana, A., Naik, S., & Nandi, P. 2023, *MNRAS*, 521, 5440, doi: [10.1093/mnras/stad867](https://doi.org/10.1093/mnras/stad867)
- Kuo, C. Y., Braatz, J. A., Condon, J. J., et al. 2011, *ApJ*, 727, 20, doi: [10.1088/0004-637X/727/1/20](https://doi.org/10.1088/0004-637X/727/1/20)
- Lammers, C., Iyer, K. G., Ibarra-Medel, H., et al. 2023, *ApJ*, 953, 26, doi: [10.3847/1538-4357/acdd57](https://doi.org/10.3847/1538-4357/acdd57)
- Liszt, H. S., & Dickey, J. M. 1995, *AJ*, 110, 998, doi: [10.1086/117579](https://doi.org/10.1086/117579)
- Lu, K.-X., Wang, J.-G., Zhang, Z.-X., et al. 2021, *The Astrophysical Journal*, 918, 50, doi: [10.3847/1538-4357/ac0c78](https://doi.org/10.3847/1538-4357/ac0c78)
- Lu, N. Y., Hoffman, G. L., Groff, T., Roos, T., & Lamphier, C. 1993, *ApJS*, 88, 383, doi: [10.1086/191826](https://doi.org/10.1086/191826)
- Maiolino, R., & Rieke, G. H. 1995, *ApJ*, 454, 95, doi: [10.1086/176468](https://doi.org/10.1086/176468)
- Maiolino, R., Russell, H. R., Fabian, A. C., et al. 2017, *Nature*, 544, 202, doi: [10.1038/nature21677](https://doi.org/10.1038/nature21677)
- Marconi, A., & Hunt, L. K. 2003, *ApJL*, 589, L21, doi: [10.1086/375804](https://doi.org/10.1086/375804)
- Marquez, I., & Moles, M. 1994, *AJ*, 108, 90, doi: [10.1086/117048](https://doi.org/10.1086/117048)
- Martin, D. C., Fanson, J., Schiminovich, D., et al. 2005, *ApJL*, 619, L1, doi: [10.1086/426387](https://doi.org/10.1086/426387)
- McHardy, I. M., Papadakis, I. E., Uttley, P., Page, M. J., & Mason, K. O. 2004, *MNRAS*, 348, 783, doi: [10.1111/j.1365-2966.2004.07376.x](https://doi.org/10.1111/j.1365-2966.2004.07376.x)
- McLure, R. J., & Dunlop, J. S. 2002, *MNRAS*, 331, 795, doi: [10.1046/j.1365-8711.2002.05236.x](https://doi.org/10.1046/j.1365-8711.2002.05236.x)
- Mountrichas, G., & Buat, V. 2023, *A&A*, 679, A151, doi: [10.1051/0004-6361/202347392](https://doi.org/10.1051/0004-6361/202347392)
- Mundell, C. G., Pedlar, A., Shone, D. L., & Robinson, A. 1999, *Monthly Notices of the Royal Astronomical Society*, 304, 481, doi: [10.1046/j.1365-8711.1999.02331.x](https://doi.org/10.1046/j.1365-8711.1999.02331.x)
- Nandi, P., Stalin, C. S., Saikia, D. J., et al. 2023a, *ApJ*, 950, 81, doi: [10.3847/1538-4357/acff1e](https://doi.org/10.3847/1538-4357/acff1e)
- . 2023b, *ApJ*, 959, 116, doi: [10.3847/1538-4357/ad0c57](https://doi.org/10.3847/1538-4357/ad0c57)
- Pan, H.-A., & Kuno, N. 2017, *ApJ*, 839, 133, doi: [10.3847/1538-4357/aa60c2](https://doi.org/10.3847/1538-4357/aa60c2)
- Papadakis, I. E., Ioannou, Z., Brinkmann, W., & Xilouris, E. M. 2008, *A&A*, 490, 995, doi: [10.1051/0004-6361:200810298](https://doi.org/10.1051/0004-6361:200810298)
- Parkash, V., Brown, M. J. I., Jarrett, T. H., & Bonne, N. J. 2018, *ApJ*, 864, 40, doi: [10.3847/1538-4357/aad3b9](https://doi.org/10.3847/1538-4357/aad3b9)
- Paturel, G., Petit, C., Prugniel, P., et al. 2003, *A&A*, 412, 45, doi: [10.1051/0004-6361:20031411](https://doi.org/10.1051/0004-6361:20031411)
- Pedlar, A., Howley, P., Axon, D. J., & Unger, S. W. 1992, *MNRAS*, 259, 369, doi: [10.1093/mnras/259.2.369](https://doi.org/10.1093/mnras/259.2.369)
- Pérez-Torres, M. A., & Alberdi, A. 2007, *MNRAS*, 379, 275, doi: [10.1111/j.1365-2966.2007.11944.x](https://doi.org/10.1111/j.1365-2966.2007.11944.x)
- Peterson, B. M., McHardy, I. M., Wilkes, B. J., et al. 2000, *ApJ*, 542, 161, doi: [10.1086/309518](https://doi.org/10.1086/309518)
- Peterson, B. M., Grier, C. J., Horne, K., et al. 2014, *ApJ*, 795, 149, doi: [10.1088/0004-637X/795/2/149](https://doi.org/10.1088/0004-637X/795/2/149)
- Pounds, K. A., Reeves, J. N., King, A. R., & Page, K. L. 2004, *MNRAS*, 350, 10, doi: [10.1111/j.1365-2966.2004.07639.x](https://doi.org/10.1111/j.1365-2966.2004.07639.x)
- Renzini, A., & Peng, Y.-j. 2015, *ApJL*, 801, L29, doi: [10.1088/2041-8205/801/2/L29](https://doi.org/10.1088/2041-8205/801/2/L29)
- Riffel, R., Dahmer-Hahn, L. G., Riffel, R. A., et al. 2022, *MNRAS*, 512, 3906, doi: [10.1093/mnras/stac740](https://doi.org/10.1093/mnras/stac740)
- Risaliti, G., Elvis, M., Fabbiano, G., Baldi, A., & Zezas, A. 2005, *ApJL*, 623, L93, doi: [10.1086/430252](https://doi.org/10.1086/430252)
- Risaliti, G., Miniutti, G., Elvis, M., et al. 2009, *ApJ*, 696, 160, doi: [10.1088/0004-637X/696/1/160](https://doi.org/10.1088/0004-637X/696/1/160)
- Rodríguez Espinosa, J. M., Rudy, R. J., & Jones, B. 1987, *ApJ*, 312, 555, doi: [10.1086/164901](https://doi.org/10.1086/164901)
- Saikia, D. J., Pedlar, A., Unger, S. W., & Axon, D. J. 1994, *MNRAS*, 270, 46, doi: [10.1093/mnras/270.1.46](https://doi.org/10.1093/mnras/270.1.46)
- Salim, S., Rich, R. M., Charlot, S., et al. 2007, *ApJS*, 173, 267, doi: [10.1086/519218](https://doi.org/10.1086/519218)
- Sánchez-Portal, M., Díaz, Á. I., Terlevich, E., & Terlevich, R. 2004, *MNRAS*, 350, 1087, doi: [10.1111/j.1365-2966.2004.07720.x](https://doi.org/10.1111/j.1365-2966.2004.07720.x)
- Sandage, A., & Bedke, J. 1994, *The Carnegie atlas of galaxies*, Vol. 638
- Sandqvist, A., Joersaeter, S., & Lindblad, P. O. 1995, *A&A*, 295, 585
- Sargent, A. J., Fischer, T. C., Johnson, M. C., et al. 2024, *ApJ*, 961, 230, doi: [10.3847/1538-4357/ad11d4](https://doi.org/10.3847/1538-4357/ad11d4)
- Sarzi, M., Rix, H.-W., Shields, J. C., et al. 2002, *ApJ*, 567, 237, doi: [10.1086/338351](https://doi.org/10.1086/338351)
- Seifina, E., Chekhtman, A., & Titarchuk, L. 2018, *A&A*, 613, A48, doi: [10.1051/0004-6361/201732235](https://doi.org/10.1051/0004-6361/201732235)
- Shin, J., Woo, J.-H., Chung, A., et al. 2019, *ApJ*, 881, 147, doi: [10.3847/1538-4357/ab2e72](https://doi.org/10.3847/1538-4357/ab2e72)
- Singh, A., Gulati, M., & Bagla, J. S. 2019, *MNRAS*, 489, 5582, doi: [10.1093/mnras/stz2523](https://doi.org/10.1093/mnras/stz2523)
- Slavcheva-Mihova, L., & Mihov, B. 2011, *A&A*, 526, A43, doi: [10.1051/0004-6361/200913243](https://doi.org/10.1051/0004-6361/200913243)
- Springob, C. M., Haynes, M. P., Giovanelli, R., & Kent, B. R. 2005, *ApJS*, 160, 149, doi: [10.1086/431550](https://doi.org/10.1086/431550)
- Stevens, I. R., Forbes, D. A., & Norris, R. P. 1999, *MNRAS*, 306, 479, doi: [10.1046/j.1365-8711.1999.02543.x](https://doi.org/10.1046/j.1365-8711.1999.02543.x)

- Storchi-Bergmann, T., & Schnorr-Müller, A. 2019, *Nature Astronomy*, 3, 48, doi: [10.1038/s41550-018-0611-0](https://doi.org/10.1038/s41550-018-0611-0)
- Sweet, S. M., Fisher, D., Glazebrook, K., et al. 2018, *ApJ*, 860, 37, doi: [10.3847/1538-4357/aabfc4](https://doi.org/10.3847/1538-4357/aabfc4)
- Tandon, S. N., Postma, J., Joseph, P., et al. 2020, *AJ*, 159, 158, doi: [10.3847/1538-3881/ab72a3](https://doi.org/10.3847/1538-3881/ab72a3)
- Terashima, Y., Kunieda, H., & Misaki, K. 1999, *PASJ*, 51, 277, doi: [10.1093/pasj/51.3.277](https://doi.org/10.1093/pasj/51.3.277)
- Tody, D. 1986, in *Society of Photo-Optical Instrumentation Engineers (SPIE) Conference Series*, Vol. 627, *Instrumentation in astronomy VI*, ed. D. L. Crawford, 733, doi: [10.1117/12.968154](https://doi.org/10.1117/12.968154)
- Tortosa, A., Bianchi, S., Marinucci, A., et al. 2018, *MNRAS*, 473, 3104, doi: [10.1093/mnras/stx2457](https://doi.org/10.1093/mnras/stx2457)
- Troyer, J., Starkey, D., Cackett, E. M., et al. 2016, *MNRAS*, 456, 4040, doi: [10.1093/mnras/stv2862](https://doi.org/10.1093/mnras/stv2862)
- Tsai, M., & Hwang, C.-Y. 2015, *AJ*, 150, 43, doi: [10.1088/0004-6256/150/2/43](https://doi.org/10.1088/0004-6256/150/2/43)
- Tueller, J., Mushotzky, R. F., Barthelmy, S., et al. 2008, *ApJ*, 681, 113, doi: [10.1086/588458](https://doi.org/10.1086/588458)
- Ulvestad, J. S., & Wilson, A. S. 1984, *ApJ*, 285, 439, doi: [10.1086/162520](https://doi.org/10.1086/162520)
- Urbanik, M., Klein, U., & Graeve, R. 1986, *A&A*, 166, 107
- Veilleux, S., Bland-Hawthorn, J., & Cecil, G. 1999, *AJ*, 118, 2108, doi: [10.1086/301095](https://doi.org/10.1086/301095)
- Véron-Cetty, M. P., & Véron, P. 2006, *A&A*, 455, 773, doi: [10.1051/0004-6361:20065177](https://doi.org/10.1051/0004-6361:20065177)
- Wang, J., Risaliti, G., Fabbiano, G., et al. 2010, *The Astrophysical Journal*, 714, 1497, doi: [10.1088/0004-637x/714/2/1497](https://doi.org/10.1088/0004-637x/714/2/1497)
- Ward, S. R., Harrison, C. M., Costa, T., & Mainieri, V. 2022, *MNRAS*, 514, 2936, doi: [10.1093/mnras/stac1219](https://doi.org/10.1093/mnras/stac1219)
- Weiler, K. W., van der Hulst, J. M., Sramek, R. A., & Panagia, N. 1981, *ApJL*, 243, L151, doi: [10.1086/183463](https://doi.org/10.1086/183463)
- Whitmore, B. C., Chandar, R., Rodríguez, M. J., et al. 2023, *ApJL*, 944, L14, doi: [10.3847/2041-8213/aca94](https://doi.org/10.3847/2041-8213/aca94)
- Williams, D. R. A., McHardy, I. M., Baldi, R. D., et al. 2017, *MNRAS*, 472, 3842, doi: [10.1093/mnras/stx2205](https://doi.org/10.1093/mnras/stx2205)
- Wolfinger, K., Kilborn, V. A., Koribalski, B. S., et al. 2013, *MNRAS*, 428, 1790, doi: [10.1093/mnras/sts160](https://doi.org/10.1093/mnras/sts160)
- Xu, C., Livio, M., & Baum, S. 1999, *AJ*, 118, 1169, doi: [10.1086/301007](https://doi.org/10.1086/301007)
- Xu, X., & Wang, J. 2022, *ApJ*, 933, 110, doi: [10.3847/1538-4357/ac7222](https://doi.org/10.3847/1538-4357/ac7222)
- Yang, T., Davé, R., Cui, W., et al. 2024, *MNRAS*, 527, 1612, doi: [10.1093/mnras/stad3223](https://doi.org/10.1093/mnras/stad3223)
- Zhang, L., & Ho, L. C. 2023, *ApJL*, 953, L9, doi: [10.3847/2041-8213/acea73](https://doi.org/10.3847/2041-8213/acea73)
- Zhuang, M.-Y., Ho, L. C., & Shangquan, J. 2021, *ApJ*, 906, 38, doi: [10.3847/1538-4357/abc94d](https://doi.org/10.3847/1538-4357/abc94d)
- Zinn, P. C., Middelberg, E., Norris, R. P., & Dettmar, R. J. 2013, *ApJ*, 774, 66, doi: [10.1088/0004-637X/774/1/66](https://doi.org/10.1088/0004-637X/774/1/66)